Chemical Engineering Science 65 (2010) 2267–2283

Contents lists available at ScienceDirect

Chemical Engineering Science

journal homepage: www.elsevier.com/locate/ces

# A fully coupled quadrature-based moment method for dilute to moderately dilute fluid–particle flows

A. Passalacqua[a,*], R.O. Fox[a], R. Garg[b], S. Subramaniam[b]

[a]Department of Chemical and Biological Engineering, Iowa State University, 2114 Sweeney Hall, Ames, IA 50011-2230, USA
[b]Department of Mechanical Engineering, Iowa State University, Black Engineering, Ames, IA 50011-2230, USA

ARTICLE INFO

*Article history:*
Received 17 April 2009
Received in revised form 18 August 2009
Accepted 1 September 2009
Available online 9 September 2009

*Keywords:*
Kinetic theory of granular flow
Quadrature-based moment methods
Computational fluid dynamics
Multiphase flow
Particle-laden channel flow

ABSTRACT

A third-order quadrature-based moment method for simulating dilute and moderately dilute fluid–particle flows has been implemented with full coupling in a computational fluid dynamics code. The solution algorithm for the particle phase uses a kinetic-based finite-volume technique to solve the velocity moment equations derived from kinetic theory. The procedure to couple the particle-phase volume-fraction and momentum equations with the Eulerian solver for the fluid phase is explained in detail. As an example application, simulations of a particle-laden vertical channel flow at fluid-phase Reynolds number 1379 and particle Stokes numbers 0.061 and 0.61 were carried out. The fluid and particle velocities, particle-phase volume fraction and granular temperature were observed to reach a steady state in the case of Stokes number 0.061, while instabilities that led to the formation of structures and initiated the particle segregation process were observed in the case with the higher Stokes number. These results are validated against results from a classical two-fluid model derived from the kinetic theory of granular flows in the small Knudsen number limit, and Euler–Lagrange simulations of the same flow.



## 1. Introduction

Dilute gas–particle flows represent an important family of multiphase flows in chemical engineering applications. A significant example is the flow in risers of circulating fluidized-bed (CFB) reactors, which were developed to increase the performance of traditional fixed bed reactors in particular fields of application like fluid catalytic cracking (FCC), catalytic combustion, coal gasification, Fischer–Tropsch synthesis, calcination processes and also elimination of pollutants and dust incineration. The success of CFB units is due to the significant increase in the contact efficiency between the phases, the reduced axial dispersion and the improved thermal control they can offer. The increasing importance of these systems underlines the need for appropriate mathematical models able to capture the complex fluid dynamical behavior of these units (Avidan, 1995; Brereton, 1995; Dry and Beeby, 1995; Grace and Bi, 1997).

Many works have been published in the literature on the mathematical modeling of risers using the two-fluid methodology (Enwald et al., 1996), with different closures to describe the particle-phase properties. Syamlal and Gidaspow (1985) and Gidaspow (1986) developed hydrodynamic models for CFB reactors, accounting for heat transfer and introducing a normal stress modulus for the particle phase to prevent the maximum particle packing limit from being exceeded. Sinclair and Jackson (1989) developed the first stationary hydrodynamic model able to predict the particulate phase stresses using moment closures derived from the kinetic theory of granular gases, as a function of the particle fluctuating energy, the so-called granular temperature. Hrenya and Sinclair (1997) studied the influence of turbulence both on the transport equations and on the kinetic theory closure equations, leading to a reformulation of the dissipation term of the granular energy, which resulted in a reduced sensitivity of the model to the value of the particle restitution coefficient. Benyahia et al. (2000) and Arastoopour (2001) simulated a FCC riser using the two-fluid approach with kinetic theory moment closures. Peirano and Leckner (1998), Peirano et al. (2002) and De Wilde et al. (2005) adopted a model that couples a two-equation turbulence model with a set of two equations for the granular temperature and for the gas–particle velocity correlation. Agrawal et al. (2001) studied the formation of meso-scale structure in high-resolution two-fluid simulations, showing that two-fluid equations predict a number of structures with higher concentration of particles, which become more and more evident as the quality of the discretization of the computational domain is improved, and underlined the importance of introducing sub-grid scale models when

* Corresponding author.
*E-mail addresses:* alberto.passalacqua@tin.it, albertop@iastate.edu (A. Passalacqua), rofox@iastate.edu (R.O. Fox).

0009-2509/$ - see front matter © 2009 Elsevier Ltd. All rights reserved.
doi:10.1016/j.ces.2009.09.002

performing coarse-grid simulations without neglecting the effect of these structures.

The two-fluid equations and the kinetic theory closures used in two-fluid models (Gidaspow, 1994; Peirano and Leckner, 1998), however, are obtained with strong assumptions on the nature of the flow, assuming that it is collisionally dominated and nearly at equilibrium, which corresponds to consider a particle-phase Knudsen number close to zero. This leads to inconsistencies and erroneous or missing predictions of physical phenomena when these models are applied to dilute fluid–particle flows, where rarefaction effects are not negligible. In order to overcome the shortcomings of two-fluid models, Simonin (1991) adopted a moment method based on the Grad (1949) approach to simulate particle-laden jets and to study non-equilibrium phenomena in dilute gas–particle flows (Sakiz and Simonin, 1998). Recently Desjardin et al. (2008) showed that two-fluid models are unable to correctly capture particle trajectory crossing, seriously compromising their ability of correctly describing any velocity moment for finite, non-zero, Stokes numbers, and clarified that the particle segregation captured by two-fluid models for finite Knudsen numbers is artificially high due to their mathematical formulation. This limitation is clearly evident in the example reported in their work of very dilute crossing jets, where a discontinuity in the velocity field originates where the jets cross each other, however, it is not limited to extremely dilute flows. In particular it can affect riser flows, where the particle volume fraction is not extremely low, but locally can be low enough to give origin to particle trajectory crossing. In the same work, Desjardin et al. shown that an approximate solution of the kinetic equation, the foundation of the kinetic theory of granular gases, can be obtained using a two-node quadrature approach, which resulted in the ability to capture particles trajectory crossing correctly for finite Stokes numbers and infinite Knudsen number. Following this approach, in this work we describe the implementation of a third-order quadrature-based moment method (Fox, 2008) in a computational fluid dynamics (CFD) code and its coupling with a fluid solver to describe fluid–particle flows. The implementation is then tested by simulating a fluid–particle flow in a vertical channel, validating the results with the predictions of a two-fluid model and Euler–Lagrange simulations of the kinetic equation.

The remainder of the paper is organized as follows. In Section 2 the equations of the computational model for the fluid and the particle phases are described. In Section 3 the implementation of the quadrature-based method and the coupling procedure with the fluid solver are explained in detail. Finally, in Section 4, the results of the simulations of a fluid–particle flow in a vertical channel are presented and discussed.

## 2. The mathematical model

In this section the governing equations of the fluid and particle phases are briefly presented. The principles of the quadrature approximation of the kinetic equation are also discussed.

### 2.1. Fluid-phase governing equations

The behavior of the fluid phase is described by the classical continuity and momentum equations solved in multi-fluid models (Drew, 1971; Syamlal et al., 1993; Gidaspow, 1994; Enwald et al., 1996). The fluid continuity equation has the form

$$\frac{\partial}{\partial t}(\alpha_\mathrm{f}\rho_\mathrm{f}) + \nabla(\alpha_\mathrm{f}\rho_\mathrm{f}\mathbf{U}_\mathrm{f}) = 0, \tag{1}$$

and the fluid momentum equation is given by

$$\frac{\partial}{\partial t}(\alpha_\mathrm{f}\rho_\mathrm{f}\mathbf{U}_\mathrm{f}) + \nabla(\alpha_\mathrm{f}\rho_\mathrm{f}\mathbf{U}_\mathrm{f}\mathbf{U}_\mathrm{f}) = \nabla(\alpha_\mathrm{f}\boldsymbol{\tau}_\mathrm{f}) - \alpha_\mathrm{f}\nabla p + \alpha_\mathrm{f}\rho_\mathrm{f}\mathbf{g} + \mathbf{M}_\mathrm{fp}, \tag{2}$$

where $\alpha_\mathrm{f}$, $\rho_\mathrm{f}$, $\mathbf{U}_\mathrm{f}$ are, respectively, the fluid-phase volume fraction, density and mean velocity, $\mathbf{M}_\mathrm{fp}$ is the momentum exchange term due to the drag between the fluid and particle phases, and $\mathbf{g}$ is the gravitational acceleration vector.

For incompressible fluids, the fluid pressure $p$ is used to satisfy the continuity equation. The fluid phase is assumed to be Newtonian, and its stress tensor $\boldsymbol{\tau}_\mathrm{f}$ is given by

$$\boldsymbol{\tau}_\mathrm{f} = \mu_\mathrm{f}(\nabla\mathbf{U}_\mathrm{f} + (\nabla\mathbf{U}_\mathrm{f})^\mathrm{T}) - \tfrac{2}{3}\mu_\mathrm{f}(\nabla\cdot\mathbf{U}_\mathrm{f})\mathbf{I}, \tag{3}$$

where $\mu_\mathrm{f}$ is the fluid dynamic viscosity and $\mathbf{I}$ the unit tensor.

### 2.2. Particle-phase governing equations

The particle phase is described assuming that particles are smooth, monodisperse, non-cohesive spheres. As a consequence, its governing equation is represented by a kinetic equation for the particle number density function $f(t,\mathbf{x},\mathbf{v})$, defined so that $f d\mathbf{x}\, d\mathbf{v}$ is the average number of particles with velocity between $\mathbf{v}$ and $\mathbf{v}+d\mathbf{v}$ and position between $\mathbf{x}$ and $\mathbf{x}+d\mathbf{x}$, at time $t$. The form of the kinetic equation is (Chapman and Cowling, 1961; Cercignani et al., 1994; Struchtrup, 2005)

$$\frac{\partial f}{\partial t} + \mathbf{v}\cdot\frac{\partial f}{\partial \mathbf{x}} + \frac{\partial}{\partial \mathbf{v}}\left(f\frac{\mathbf{F}}{m_\mathrm{p}}\right) = \mathbb{C}, \tag{4}$$

where $\mathbb{C}$ represents the rate of change in the number density function due to binary collisions between the particles, and $\mathbf{F}$ is the force acting on each particle, which includes gravity and drag.[1] It is worth noting that the quadrature-based moment method developed in this work can be applied to more complicated forms of the kinetic equation (e.g., aggregation, diffusion in velocity space, etc.). For each new case, it suffices to derive the moment equations starting from the kinetic equation.

In this work the collision term $\mathbb{C}$ is described using the Bhatnagar–Gross–Krook collision operator (Bhatnagar et al., 1954):

$$\mathbb{C} = \frac{1}{\tau_\mathrm{c}}(f_\mathrm{es} - f), \tag{5}$$

where $\tau_\mathrm{c}$ is the collision time and $f_\mathrm{es}$ is the equilibrium distribution function, extended to account for inelastic collisions:

$$f_\mathrm{es} = \frac{N}{[\det(2\pi\boldsymbol{\lambda})]^{1/2}}\exp\left(-\frac{1}{2}(v_{\mathrm{p},i} - U_{\mathrm{p},i})\lambda^{-1}(v_{\mathrm{p},j} - U_{\mathrm{p},j})\right), \tag{6}$$

where $\boldsymbol{\lambda}^{-1}$ is the inverse of the matrix $\boldsymbol{\lambda}$, defined by

$$\boldsymbol{\lambda} = \gamma\omega^2\Theta\mathbf{I} + (\gamma\omega^2 - 2\gamma\omega + \mathbf{I})\boldsymbol{\sigma} \tag{7}$$

with $\gamma = 1/Pr$, and $\omega = (1+e)/2$, being $N$ the number density of particles (zero-order moment), $\mathbf{U}_\mathrm{p}$ the mean particle velocity (first-order moment), $e$ the restitution coefficient, $\Theta_\mathrm{p}$ the granular temperature, and $\boldsymbol{\sigma}$ the velocity covariance matrix. In this work $\gamma = 1$, being $Pr = 1$ in the standard BGK model (Struchtrup, 2005).

The expression for the collision operator in Eq. (5) represents a linear approximation of the complete Boltzmann collision integral, valid under the assumption of collision-dominated flows with $e$ near unity. However, any closed collision kernel, including the full Boltzmann collision integral valid for arbitrary $e$, can be used with the procedure presented in this work (Fox, 2008).

A convenient approach to solve the Boltzmann equation, as an alternative to the expensive direct solvers (Beylich, 2000; Carrillo

[1] Only the drag force and the gravity are considered here. Thus, we are implicitly assuming that the particles are much denser than the fluid. However, $\mathbf{F}$ can include other forces such as, for example, buoyancy and electrostatic forces acting on the particles.

et al., 2007) and Lagrangian methods (Bird, 1994), is to consider a set of moments of the distribution function $f$ (Struchtrup, 2005), and track their evolution in space and time, instead of aiming at reconstructing the exact shape of $f$. This leads to an approximate solution of the kinetic equation, which is, however, satisfactory for many engineering applications, like the simulation of granular flows and fluid–particle flows.

In this work a set of 20 moments $W^3$ of $f$ up to the third order defined by

$$W^3 = (M^0, M_1^1, M_2^1, M_3^1, M_{12}^2, M_{13}^2, M_{22}^2, M_{23}^2, M_{33}^2, M_{111}^3, M_{112}^3, M_{113}^3, M_{122}^3, M_{123}^3, M_{133}^3, M_{222}^3, M_{223}^3, M_{233}^3, M_{333}^3)$$

is considered, where the superscripts represent the order of the corresponding moment (Fox, 2008). Each moment is defined through integrals of the distribution function as

$$M^0 = \int f \, d\mathbf{v}, \quad M_i^1 = \int v_i f \, d\mathbf{v},$$

$$M_{ij}^2 = \int v_i v_j f \, d\mathbf{v}, \quad M_{ijk}^3 = \int v_i v_j v_k f \, d\mathbf{v}. \tag{8}$$

Note that the particle-phase volume fraction $\alpha_\mathrm{p}$ and mean particle velocity $\mathbf{U}_\mathrm{p}$ are related to these moments by

$$\alpha_\mathrm{p} = V_\mathrm{p} M^0 \tag{9}$$

and

$$\rho_\mathrm{p} \alpha_\mathrm{p} U_{\mathrm{p},i} = m_\mathrm{p} M_i^1, \tag{10}$$

where $m_\mathrm{p} = \rho_\mathrm{p} V_\mathrm{p}$ is the mass of a particle with density $\rho_\mathrm{p}$ and volume $V_\mathrm{p} = \pi d_\mathrm{p}^3/6$. In this work, $m_\mathrm{p}$ is constant. Likewise, the particle temperature is defined in terms of the trace of the particle velocity covariance matrix, which is found from $M_{ij}^2$ and lower-order moments. By definition, $\alpha_\mathrm{f} + \alpha_\mathrm{p} = 1$ and this relation must be accounted for when solving a fully coupled system for the fluid and particle phases.

The application of the definition of the moments to both sides of Eq. (4) allows the moment transport equations to be derived. If the force acting on each particle is divided into two components, one due to the drag and the other due to gravity, the set of 20 transport equations, one for each moment in $W^3$ is given by

$$\begin{aligned}
&\frac{\partial M^0}{\partial t} + \frac{\partial M_i^1}{\partial x_i} = 0,\\
&\frac{\partial M_i^1}{\partial t} + \frac{\partial M_{ij}^2}{\partial x_j} = A_i^1 + g_i M^0,\\
&\frac{\partial M_{ij}^2}{\partial t} + \frac{\partial M_{ijk}^3}{\partial x_k} = C_{ij}^2 + A_{ij}^2 + g_i M_j^1 + g_j M_i^1,\\
&\frac{\partial M_{ijk}^3}{\partial t} + \frac{\partial M_{ijkl}^4}{\partial x_l} = C_{ijk}^3 + A_{ijk}^3 + g_i M_{jk}^2 + g_j M_{ik}^2 + g_k M_{ij}^2,
\end{aligned} \tag{11}$$

where $A_i^1$, $A_{ij}^2$ and $A_{ijk}^3$ are the source terms due to the acceleration acting on each particle, while $C_{ij}^2$ and $C_{ijk}^3$ are those due to the collision operator. It is worth noting that the force term only affects the moments of order higher than zero, because it is assumed that the number density of the particles is conserved. Also, the collision term only influences the moments of order higher than one, because of the assumption that collisions do not change the particle number density (no aggregation and breakage phenomena), and do not influence the mean momentum of the particle phase. In general, the conservative equations for the particle phase needed for coupling with the fluid phase are found by multiplying the expressions in Eq. (11) by $m_\mathrm{p}$. For simplicity, hereinafter we will assume that all of the velocity moments have been multiplied by $V_\mathrm{p}$, so that the zero order moment corresponds to the particle phase volume fraction $M^0 = \alpha_\mathrm{p}$.

The set of transport equations (11) is not closed, because each equation contains the spatial fluxes of the moments of order immediately higher, and the source terms due to the drag force and to collisions. As a consequence, closures have to be provided for these terms. In quadrature-based moment methods Gaussian quadrature formulas are used to provide closures to the source terms in the moment transport equations by introducing a set $V_\beta$ of $\beta$ weights $n_\alpha$ and abscissas $\mathbf{U}_\alpha$, which are determined from the moments of the distribution function using an inversion algorithm, and approximating the distribution function with a sum of Dirac delta functions:

$$f(\mathbf{v}) = \sum_{\alpha=1}^{\beta} n_\alpha \delta(\mathbf{v} - \mathbf{U}_\alpha). \tag{12}$$

In the following discussion we will consider a set of $\beta = 8$ weights and abscissa $V_8$ per each velocity component, which are obtained by considering two quadrature nodes in each direction of velocity phase space. The inversion algorithm to obtain $V_8$ from the set of moments $W^3$ is explained in detail in Fox (2008) and summed up in Appendix A. Once the weights and abscissas are known, the moments can be computed as a function of the quadrature weights and abscissas by approximating the integrals in Eq. (8) with summations:

$$\begin{aligned}
&M^0 = \sum_{\alpha=1}^{\beta} n_\alpha, \quad M_i^1 = \sum_{\alpha=1}^{\beta} n_\alpha U_{\alpha i},\\
&M_{ij}^2 = \sum_{\alpha=1}^{\beta} n_\alpha U_{\alpha i} U_{\alpha j}, \quad M_{ij}^3 = \sum_{\alpha=1}^{\beta} n_\alpha U_{\alpha i} U_{\alpha j} U_{\alpha k}.
\end{aligned} \tag{13}$$

The source terms due to drag and gravity are computed as

$$\begin{aligned}
&A_i^1 = \sum_{\alpha=1}^{\beta} n_\alpha \left( \frac{F_{i\alpha}^\mathrm{D}}{m_\mathrm{p}} + g_i \right),\\
&A_{ij}^2 = \sum_{\alpha=1}^{\beta} n_\alpha \left[ \left( \frac{F_{i\alpha}^\mathrm{D}}{m_\mathrm{p}} + g_i \right) U_{j\alpha} + \left( \frac{F_{j\alpha}^\mathrm{D}}{m_\mathrm{p}} + g_j \right) U_{i\alpha} \right],\\
&A_{ijk}^3 = \sum_{\alpha=1}^{\beta} n_\alpha \left[ \left( \frac{F_{i\alpha}^\mathrm{D}}{m_\mathrm{p}} + g_i \right) U_{j\alpha} U_{k\alpha} + \left( \frac{F_{j\alpha}^\mathrm{D}}{m_\mathrm{p}} + g_j \right) U_{k\alpha} U_{i\alpha} \right.\\
&\qquad \left. + \left( \frac{F_{k\alpha}^\mathrm{D}}{m_\mathrm{p}} + g_k \right) U_{i\alpha} U_{j\alpha} \right],
\end{aligned} \tag{14}$$

where the drag force terms are computed as

$$\mathbf{F}_\alpha^\mathrm{D} = \frac{m_\mathrm{p}}{\tau_\alpha^\mathrm{D}} (\mathbf{U}_\mathrm{f} - \mathbf{U}_\alpha) = K_{\mathrm{fp},\alpha}^{\mathrm{QMOM}} (\mathbf{U}_\mathrm{f} - \mathbf{U}_\alpha), \tag{15}$$

with the drag time for each abscissa given by

$$\tau_\alpha^\mathrm{D} = \frac{4 d_\mathrm{p} \rho_\mathrm{p}}{3 \alpha_\mathrm{f} \rho_\mathrm{f} C_\mathrm{D}(Re_{\mathrm{p}\alpha}, \alpha_\mathrm{f}) |\mathbf{U}_\mathrm{f} - \mathbf{U}_\alpha|}. \tag{16}$$

The particle Reynolds number for each abscissa is defined by[2]

$$Re_{\mathrm{p}\alpha} = \frac{\rho_\mathrm{f} d_\mathrm{p} |\mathbf{U}_\mathrm{f} - \mathbf{U}_\alpha|}{\mu_\mathrm{f}}, \tag{17}$$

[2] A mean particle Reynolds number can be defined by

$$Re_\mathrm{p} = \frac{1}{M^0} \sum_{\alpha=1}^{\beta} n_\alpha Re_{\mathrm{p}\alpha}.$$

.

and the drag coefficient $C_D$ is provided by the Schiller and Naumann (1935) correlation, modified to account for moderately dense flows ($\alpha_f > 0.8$) as in Wen and Yu (1966):

$$C_D(Re_p, \alpha_f) = \frac{24}{\alpha_f Re_p}[1 + 0.15(\alpha_f Re_p)^{0.687}]\alpha_f^{-2.65}. \quad (18)$$

It is worth underlining that in the evaluation of the force term, the relative velocity vector $\mathbf{U}_f - \mathbf{U}_\alpha$ is defined as a function of the quadrature abscissas $\mathbf{U}_\alpha$, instead of the mean particle velocity. As a consequence, the drag time and the drag force have different values for each quadrature node. Note also that for small $Re_p$ (i.e., the Stokes flow limit), the drag coefficient reduces to $C_D(Re_p, \alpha_f) = 24/(\alpha_f^{3.65} Re_p)$ and $\tau_\alpha^D$ will be the same for all abscissas.

For collisions, the source terms in the moment transport equations are given by

$$C_{ij}^2 = \frac{\alpha_p}{\tau_c}(\lambda_{ij} - \sigma_{ij}),$$

$$C_{ijk}^3 = \frac{1}{\tau_c}(\Lambda_{ijk} - M_{ijk}^3). \quad (19)$$

For hard-sphere collisions, the collision time is defined by

$$\tau_c = \frac{\pi^{1/2} d_p}{12 \alpha_p g_0 \Theta^{1/2}}, \quad (20)$$

with the granular temperature $\Theta$ defined in terms of the moments by

$$\Theta = \tfrac{1}{3}(\sigma_{11} + \sigma_{22} + \sigma_{33}), \quad (21)$$

where

$$\sigma_{11} = \frac{M_{11}^2}{M^0} - \left(\frac{M_1^1}{M^0}\right)^2,$$

$$\sigma_{22} = \frac{M_{22}^2}{M^0} - \left(\frac{M_2^1}{M^0}\right)^2,$$

$$\sigma_{33} = \frac{M_{33}^2}{M^0} - \left(\frac{M_3^1}{M^0}\right)^2. \quad (22)$$

In Eq. (20), $g_0$ is the radial distribution function, which depends on $\alpha_p$, and is used to account for the increased collision frequency in moderately dense flows. In this work, we use the model proposed by Carnahan and Starling (1969):

$$g_0 = \frac{1}{1 - \alpha_p} + \frac{3\alpha_p}{2(1 - \alpha_p)^2} + \frac{\alpha_p^2}{2(1 - \alpha_p)^3}. \quad (23)$$

For the dilute flow considered in Section 4, $g_0 \approx 1$. It is worth recalling that in the kinetic equation all particle–particle interactions (e.g., particle pressure, particle viscosity, etc.) are described by the collision term. Hence, there is no need to add additional terms in the moment transport equations to describe such processes. Finally, recall that in the derivation of the two-fluid model, the collision time is assumed to be much smaller than all other time scales in the flow (i.e., the particle-phase Knudsen number is assumed to be small). By solving directly for the velocity moments, no such assumptions are made in quadrature-based moment methods. However, for small values of the Knudsen number, when the radial distribution function becomes large, the two-fluid model will be computationally more efficient because the fast collision time scales are replaced by constitutive equations for the stresses and energy flux. A comparison of the computational times required to perform the simulations considered in this work is reported in Appendix D.

An important point for obtaining a stable solution to the moment transport equations is represented by the closure provided for the moment spatial fluxes. These fluxes are represented by the second term on the left-hand side of Eq. (11), and are computed according to their kinetic definition (Perthame, 1990; Desjardin et al., 2008; Fox, 2008). First each moment involved in the expression for the fluxes is decomposed into two contributions, as shown in Eq. (24) for the zero-order moment, whose spatial flux involves the first-order moments:

$$M_i^1 = \int_{-\infty}^{0} v_i \left(\int f \, dv_j \, dv_k\right) dv_i + \int_{0}^{+\infty} v_i \left(\int f \, dv_j \, dv_k\right) dv_i. \quad (24)$$

The integrals are then approximated using the Dirac-delta representation of the distribution function $f$ leading to

$$M_i^1 = \sum_{\alpha=1}^{\beta} n_\alpha \min(0, U_{i\alpha}) + \sum_{\alpha=1}^{\beta} n_\alpha \max(0, U_{i\alpha}). \quad (25)$$

In a similar manner, the decomposition is applied to all other moments, to compute the fluxes as a function of the weights and abscissas. This procedure to evaluate the spatial fluxes is essential to ensure the realizability of the set of moments by means of the quadrature approximation, or, in other words, that the set of weights and abscissas actually represent a real distribution function. It is worth to notice that the third-order moment spatial flux depends on fourth-order moments, which are not provided by the solution of the transport equations (11). Closures for $M_{ijkl}^4$ are obtained in terms of the quadrature representation of the distribution function as (Fox, 2008)

$$M_{ijkl}^4 = \sum_{\alpha=1}^{\beta} n_\alpha U_{\alpha i} U_{\alpha j} U_{\alpha k} U_{\alpha l}. \quad (26)$$

The explicit closure for the third-order moments spatial fluxes is implicit in Eqs. (28) and (29).

As the reader might have noticed, the QMOM procedure proposed in Fox (2008) and summarized here, significantly differs from the quadrature method of moments applied to population balance equations (Marchisio and Fox, 2003) due to the different nature of the velocity distribution function with respect to the particle size distribution. In the problem addressed in this work, the spatial transport involves the quadrature abscissas, requiring special treatment in the evaluation of the moment spatial fluxes, while in the case of a particle size distribution, weights and abscissas are transported as passive scalars.

## 3. Implementation in a CFD code

The quadrature-based moment method discussed in the previous section has been implemented in the MFIX (Syamlal et al., 1993) multiphase computational fluid dynamics (CFD) code and fully coupled with its solver for the fluid phase, to simulate fluid–particle flows. We will refer to the resulting simulation code as MFIX-QMOM. The two-fluid model in MFIX uses the finite-volume approach (Ferziger and Peric, 2002) on a structured computational grid with fully staggered arrangement of pressure and velocity, with the velocity stored at the cell-face centers, and the pressure stored at cell centers. The moment transport equations (Eqs. (11)) are solved using a similar arrangement, with all the variables stored at the cell centers, because the staggered arrangement is not necessary since the pressure gradient is absent from the equations and hence the risk of the checkerboarding effect is absent. As a consequence, the difference in the locations at which the velocities are stored has to be accounted for when the coupling between the phases is implemented. In particular, the QMOM algorithm needs the fluid-phase velocity at the cell

center, which is obtained by interpolating the values provided by the MFIX fluid solver at the cell-face centers. Vice-versa, the drag force provided to the fluid solver has to be computed as a function of the particle velocities on the cell-face centers, which are computed by interpolating the cell-centered values provided by the QMOM solver.

### 3.1. Solution of the fluid-phase equations

The fluid-phase equations are solved using the SIMPLE algorithm (Patankar, 1980) with the partial elimination procedure (Spalding, 1980) to deal with the coupling term due to the drag, as described in detail in Syamlal (1998). The fluid-phase volume fraction is provided from the solution to the moment transport equations. In practice, the coupling between the two solvers is very similar to that used in discrete element methods (DEM) for fluid–particle flows. An important difference with DEM is, however, the absence of statistical noise in the QMOM solver. This generally leads to faster convergence of the fluid-phase solver than in DEM simulations.

### 3.2. Solution of the moment transport equations

The moment transport equations (Eqs. (11)) are discretized according to the finite-volume technique, using a second-order Runge–Kutta scheme for time integration. Before proceeding with the description of the QMOM solver, it is worth reiterating that the moment transport equations are rescaled so that the zero-order moment $M^0$ represents the particle-phase volume fraction instead of the number density. This operation is important to ensure the stability and accuracy of the quadrature-inversion algorithm, which would be compromised by the high round-off error caused by the computation in terms of the number density. As noted earlier, the scaling of the equations is simply performed by multiplying them by the particle volume $V_\mathrm{p}$, and by modifying the collision and drag terms accordingly. After this rescaling, the collision time $\tau_\mathrm{c}$ and drag time $\tau_\alpha^\mathrm{D}$ are unchanged. The rescaled weights $n_\alpha$ can then be interpreted as representing the volume fraction of the corresponding abscissa.

The steps in the QMOM solver for the solution of the moment transport equations can be summed up as follows:

1. Initialize weights and abscissas in $V_8$.
2. Compute the moments in $W^3$ using Eq. (13). Note that it is not necessary to initialize the moments directly, because they can be computed as a consequence of the specified weights and abscissas.
3. Advance the moments in $W^3$ over a half time step $\Delta t/2$, and, using a time-split procedure:
   - account for the spatial fluxes,
   - account for collisions,
   - account for the body and drag forces acting on particles,
   - apply boundary conditions.
4. Apply the inversion algorithm to the new set of moments to compute the updated weights and abscissas.
5. Recompute the moments from the weights and abscissas using Eq. (13), performing the projection step (Fox, 2008), necessary to ensure that the transported moments are consistent with their quadrature representation.
6. Advance the moments over a half time step $\Delta t/2$ and repeat the same operations performed from steps 3 to 5 for the full time step.
7. Repeat from step 3.

The time step used in the QMOM solver is evaluated on the basis of the collision time $\tau_\mathrm{c}$, the drag time $\tau^\mathrm{D}$, and the Courant number based on the maximum abscissas in the whole computational domain to ensure the stability of the solution. The key steps in the algorithm are illustrated in detail in the following subsections. Note that, due to hyperbolic nature of the moment transport equations, it is theoretically possible to use a CFL number of unity without losing stability. Thus the QMOM solver will be particularly efficient for flows where the collision time does not control the time step (i.e., sufficiently large Knudsen number). In such cases, the efficiency of the gas-phase flows solver will be critical for the overall efficiency.

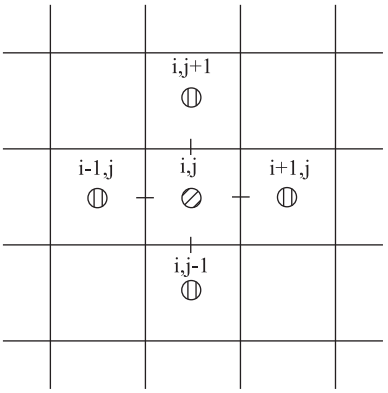


**Fig. 1.** Schematic representation of a computational cell to illustrate how the moment spatial fluxes are computed.

### 3.3. Computation of the moment spatial fluxes

The moment spatial fluxes are computed as a function of the quadrature weights and abscissas, following their kinetic definition, as discussed earlier. To explain how the computation of the fluxes is performed, let us consider the computational cell in Fig. 1, and introduce four sets of weights and abscissas: $V^-_{\beta,l}$, $V^+_{\beta,l}$, $V^-_{\beta,r}$, $V^+_{\beta,r}$. These sets of weights and abscissa are found by interpolating the cell-centered values of the weights and abscissa on the faces of the computational cell. If we consider the horizontal direction in Fig. 1 and adopt a first-order scheme, we have

$$
\begin{aligned}
V^-_{\beta,l} &= \{n^-_{\alpha,l} = n^{i-1,j}_\alpha; \mathbf{U}^-_{\alpha,l} = \mathbf{U}^{i-1,j}_\alpha\},\\
V^+_{\beta,l} &= \{n^+_{\alpha,l} = n^{i,j}_\alpha; \mathbf{U}^+_{\alpha,l} = \mathbf{U}^{i,j}_\alpha\},\\
V^-_{\beta,r} &= \{n^-_{\alpha,r} = n^{i,j}_\alpha; \mathbf{U}^-_{\alpha,r} = \mathbf{U}^{i,j}_\alpha\},\\
V^+_{\beta,r} &= \{n^+_{\alpha,r} = n^{i+1,j}_\alpha; \mathbf{U}^+_{\alpha,r} = \mathbf{U}^{i+1,j}_\alpha\}.
\end{aligned}
\tag{27}
$$

At this point the two Riemann fluxes at the left and right cell faces, $G_l$ and $G_r$, are computed as follows:

$$
\begin{aligned}
G_{1,l} = &\sum_{\alpha=1}^{\beta} n^-_{\alpha,l} \max(0, U^-_{1\alpha l}) \begin{pmatrix} 1 \\ U^-_{i\alpha l} \\ U^-_{i\alpha l} U^-_{j\alpha l} \\ U^-_{i\alpha l} U^-_{j\alpha l} U^-_{k\alpha l} \end{pmatrix} \\
&+ \sum_{\alpha=1}^{\beta} n^+_{\alpha,l} \min(0, U^+_{1\alpha l}) \begin{pmatrix} 1 \\ U^+_{i\alpha l} \\ U^+_{i\alpha l} U^+_{j\alpha l} \\ U^+_{i\alpha l} U^+_{j\alpha l} U^+_{k\alpha l} \end{pmatrix},
\end{aligned}
\tag{28}
$$

$$G_{1,r} = \sum_{\alpha=1}^{\beta} n^{-}_{\alpha,r} \max(0, U^{-}_{1\alpha r}) \begin{pmatrix} 1 \\ U^{-}_{i\alpha r} \\ U^{-}_{i\alpha r} U^{-}_{j\alpha r} \\ U^{-}_{i\alpha r} U^{-}_{j\alpha r} U^{-}_{k\alpha r} \end{pmatrix} + \sum_{\alpha=1}^{\beta} n^{+}_{\alpha,l} \min(0, U^{+}_{1\alpha r}) \begin{pmatrix} 1 \\ U^{+}_{i\alpha r} \\ U^{+}_{i\alpha r} U^{+}_{j\alpha r} \\ U^{+}_{i\alpha r} U^{+}_{j\alpha r} U^{+}_{k\alpha r} \end{pmatrix}, \tag{29}$$

and the net flux in the horizontal direction is then computed as

$$G_1 = G_{1,r} - G_{1,l}. \tag{30}$$

Using a similar procedure, it is possible to compute the moment spatial fluxes in each direction, thereby obtaining the flux vector $\mathbf{G} = \{G_1, G_2, G_3\}$. The moments are then updated as a consequence of their spatial fluxes by solving the ODE

$$\frac{dW^3}{dt} = \mathbf{G} \tag{31}$$

in each computational cell of the domain under consideration.

### 3.4. Computation of force contributions

The contributions to the evolution of the moments in $W^3$ due to the forces acting on each particle are directly computed, operating on the weights and abscissas of the quadrature approximation, by solving a set of two ODEs:

$$\frac{dn_\alpha}{dt} = 0,$$
$$\frac{dU_{i\alpha}}{dt} = \frac{F_{i\alpha}}{m_\mathrm{p}} + g_i, \tag{32}$$

written considering that the body and drag forces do not affect the quadrature weights because they do not change the number of the particles, and only influence the abscissas.

### 3.5. Contribution of collisions

Collisions are accounted for by resolving the differential equation for the change in the moments due to collisions:

$$\frac{dW^3}{dt} = C(W^3), \tag{33}$$

where $C(W^3)$ is provided by Eq. (19).

### 3.6. Boundary conditions

The boundary conditions for the moment transport equations can be specified either in terms of the moments, or in terms of the weights and abscissas of the quadrature. The latter approach is often more convenient due to its simplicity. In this work periodic and wall-reflective boundary conditions are considered. Periodic boundary conditions, where $H$ is the length of the system in the periodic direction, are specified in terms of the quadrature weights and abscissas as

$$V_{\beta,0} = V_{\beta,H}, \tag{34}$$

where $V_{\beta,0}$ and $V_{\beta,H}$ are the set of weights and abscissas in each cell of the two periodic boundaries of the computational domain. Once the weights and abscissas are set, the moments at the periodic boundaries can be computed by means of Eq. (13).

Specularly reflective walls, with particle–wall restitution coefficient $e_\mathrm{w}$, are described by

$$\begin{pmatrix} n_\alpha \\ U_{1,\alpha} \\ U_{2,\alpha} \\ U_{3,\alpha} \end{pmatrix}_{i=0} = \begin{pmatrix} n_\alpha / e_\mathrm{w} \\ U_{1,\alpha} \\ -e_\mathrm{w} U_{2,\alpha} \\ U_{3,\alpha} \end{pmatrix}_{i=1}, \tag{35}$$

which is written considering a planar wall perpendicular to the second direction of the reference frame, located at position $i=0$, where $i=1$ represents the computational cell neighboring the wall. Note that other types of boundary conditions used in Lagrangian simulations (e.g., diffuse walls) can be easily accommodated using quadrature.

### 3.7. Phase coupling

The coupling between the fluid and particle phases is obtained by means of the momentum exchange term in the fluid momentum equation and the drag term included in the moment transport equations. The momentum exchange term in the fluid phase is written as a function of the quadrature weights and abscissas:

$$\mathbf{M}_\mathrm{fp} = \sum_{\alpha=1}^{\beta} n_\alpha K_{\mathrm{fp},\alpha} (\mathbf{U}_\alpha - \mathbf{U}_\mathrm{f}), \tag{36}$$

where $K_{\mathrm{fp},\alpha} = K^{\mathrm{QMOM}}_{\mathrm{fp},\alpha} / V_\mathrm{p}$. A direct solution of the fluid-phase momentum Eq. (2), with the drag term treated as an explicit source term is possible when the particle mass loading $\xi = \alpha_\mathrm{p}\rho_\mathrm{p}/(\alpha_\mathrm{f}\rho_\mathrm{f})$ is small, and the drag force is not too strong. This procedure, however, can lead to difficult or impossible convergence of iterative solvers when the particle mass loading is high, and, as a consequence, the drag effect is strong (Oliveira and Issa, 1994; Karema and Lo, 1999). To avoid this problem Spalding (1980) proposed the partial elimination algorithm (PEA), which consists in a manipulation of the momentum equations of the two phases in order to eliminate the velocity of the particle phase from the fluid-phase momentum equation and vice versa. This procedure needs to be modified when QMOM is used to describe the particle phase, because the mean momentum equation for the dispersed phase is not solved directly.

The modified PEA procedure is illustrated here for the case of a fluid phase and a single particle phase. The extension to an arbitrary number of particle phases is straightforward. To start the derivation of the method, let us consider the semi-discretized fluid momentum equation written in finite-volume notation (Ferziger and Peric, 2002), and a semi-discretized momentum equation for the virtual particle phase, represented by a single quadrature abscissa:

$$A^\mathrm{P}_\mathrm{f} U^\mathrm{P}_\mathrm{f} + \sum_f A^f_\mathrm{f} U^f_\mathrm{f} = S_\mathrm{f} - \alpha_\mathrm{f} \nabla p + \sum_{\alpha=1}^{\beta} K_{\mathrm{fp},\alpha} (U^\mathrm{P}_\alpha - U^\mathrm{P}_\mathrm{f}), \tag{37}$$

$$A^\mathrm{P}_\alpha U^\mathrm{P}_\alpha + \sum_f A^f_\alpha U^f_\alpha = S_\alpha + K_{\mathrm{fp},\alpha} (U^\mathrm{P}_\mathrm{f} - U^\mathrm{P}_\alpha), \tag{38}$$

where $A^\mathrm{P}_\mathrm{f}$ and $A^\mathrm{P}_\mathrm{f}$ are the central coefficients, $U^\mathrm{P}_\mathrm{f}$ and $U^\mathrm{P}_\alpha$ are at the cell center, $S_\mathrm{f}$ and $S_\alpha$ are the source terms and $^f$ indicates the contributions of the neighboring cells. It is convenient to define the quantities

$$H_\mathrm{f} = S_\mathrm{f} - \sum_f A^f_\mathrm{f} U^f_\mathrm{f},$$
$$H_\alpha = S_\alpha - \sum_f A^f_\alpha U^f_\alpha, \tag{39}$$

and to substitute them into Eqs. (37) and (38), obtaining

$$A_f^P U_f^P = H_f - \alpha_f \nabla p + \sum_{\alpha=1}^{\beta} K_{fp,\alpha}(U_\alpha^P - U_f^P), \tag{40}$$

$$A_\alpha^P U_\alpha^P = H_\alpha + K_{fp,\alpha}(U_f^P - U_\alpha^P). \tag{41}$$

By solving Eq. (41) for $U_\alpha^P$, an expression for the particle velocity abscissa is found:

$$U_\alpha^P = \eta_\alpha (H_\alpha + K_{fp,\alpha} U_f^P),$$

$$\eta_\alpha = \frac{1}{A_\alpha^P + K_{fp,\alpha}}, \tag{42}$$

which, substituted into Eq. (40), gives an expression for the fluid velocity, where the effect of the particle phase is eliminated:

$$U_f = \eta_f \left( H_f - \alpha_f \nabla p + \sum_{\alpha=1}^{\beta} K_{fp,\alpha} \eta_\alpha H_\alpha \right),$$

$$\eta_f = \frac{1}{A_f^P + \sum_{\alpha=1}^{\beta} \eta_\alpha K_{fp,\alpha} A_\alpha^P}. \tag{43}$$

The expression for the velocity in Eq. (43) is then used to compute the fluid-phase mass flux $\varphi_f = \alpha_f \rho_f U_f$ to be used in the derivation of the pressure equation:

$$\nabla \cdot \varphi_f = 0, \tag{44}$$

which can be rewritten as

$$\nabla \cdot (\rho_f \eta_\alpha \alpha_f^2 \nabla p) = \nabla \cdot \left[ \alpha_f \rho_f \eta_f \left( H_f + \sum_{\alpha=1}^{\beta} \eta_\alpha K_{fp,\alpha} H_\alpha \right) \right]. \tag{45}$$

The solution to Eq. (45) provides the updated fluid pressure field, on the basis of which the fluid velocity estimated using Eq. (43) has to be corrected to respect the continuity constraint.

## 4. Simulation of fluid–particle flow in a vertical channel

Simulations of a fluid–particle flow in a periodic vertical channel (Fig. 2), constituted by two plane parallel walls separated by a distance $D$ and length $H$, were performed considering fluid and particle phases whose properties are given in Table 1. The mass flow rate of the fluid phase, and hence the average fluid velocity $\overline{U}_f$, was fixed so that the Reynolds number of the fluid phase is lower than its transition value to turbulence for a single-phase flow between two parallel plates, where the transition to turbulence occurs near $Re_f = \rho_f \overline{U}_f D/\mu_f \approx 1500$. This limit was respected by setting $Re_f = 1379$ using the fluid viscosity $\mu_f$ (i.e., the fluid was more viscous than air at room temperature by a factor of 10). The other physical properties were chosen to be typical of gas–solid riser flows. Alternatively, one could use the properties of air and decrease the gravitational constant in order to keep the particles suspended at a given $Re_f$. With these physical properties, the average fluid velocity, averaged over the direction normal to the channel walls, was $\overline{U}_f = 2$ m/s. The particle phase was initialized with zero velocity and a uniform volume fraction in all computational cells equal to 0.04. No-slip boundary conditions at the walls were imposed for the fluid phase in all the simulations. In order to validate the MFIX-QMOM code, two-fluid simulations were performed using the standard kinetic theory implementation in MFIX (Syamlal et al., 1993), solving the transport equation for the granular temperature, and using Johnson and Jackson (1987) boundary conditions for both the particle velocity and the granular temperature. A summary of the two-fluid model equations can be found in Appendix C. Perfectly elastic collisions were assumed between particles and walls, along with a zero specularity coefficient to mimic specularly reflective walls,[3] consistent with the MFIX-QMOM simulations. A restitution coefficient of $e = 1$ was used for particle–particle collisions. Gravity was assumed to act in the downward direction, opposed to the fluid motion, with magnitude $g = 9.81$ m/s$^2$. Two values of the particle Stokes number ($St = 0.061$, 0.61), defined by

$$St = \frac{\rho_p d_p^2 \overline{U}_f}{18 \mu_f D}, \tag{46}$$

were considered by changing the particle diameter $d_p$. In the following, we refer to $St = 0.061$ as the low-Stokes-number flow, and $St = 0.61$ as the finite-Stokes-number flow. Frictional stresses were neglected in all the simulations, because they can be assumed negligible in the range of volume fractions considered in this work (Johnson and Jackson, 1987). In all the simulations, the effect of the volume occupied by the particles is accounted for in the equations for the fluid phase; however, for the low-Stokes-number flow both a case with partial coupling (no effect of the particles drag on the fluid momentum) and with full coupling are considered for the MFIX-QMOM simulations. By default, the two-fluid model in MFIX has full momentum coupling, and comparisons with MFIX-QMOM are made using full coupling and the same correlations for the drag law and for $g_0$. For the finite-Stokes-number flow, Euler–Lagrange simulations were performed using the improved Lagrangian method described in Garg et al. (2007, 2009). For these simulations, the collision kernel of Schmidt and Rutland (2000) was used with $g_0 = 1$, along with the Schiller and Naumann (1935) drag law (corresponding to $C_D(Re_p, \alpha_f = 1)$). Thus, comparisons between Euler–Lagrange and MFIX-QMOM simulations

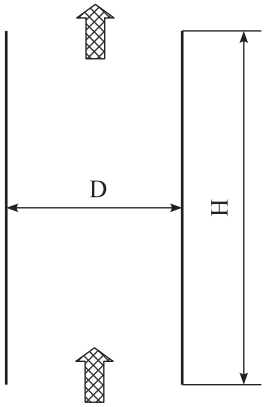


**Fig. 2.** Schematic representation of the two-dimensional channel considered in the simulations.

**Table 1**
Physical properties used in the channel-flow simulations.

| Property | Value |
|---|---|
| $D$ (m) | 0.1 |
| $d_p$ (μm) | 80, 252.9 |
| $\mu_f$ (Pa s) | $1.74 \times 10^{-4}$ |
| $e$ | 1.0 |
| $H$ (m) | 1.0 |
| $\rho_f$ (kg/m$^3$) | 1.2 |
| $\rho_p$ (kg/m$^3$) | 1500 |
| $e_w$ | 1.0 |

[3] The assumption corresponds to applying a free-slip boundary condition for the particle phase.

are done with $g_0 = 1$ and $C_D(Re_p, 1)$. Note that for the low-Stokes-number flow, the Euler–Lagrange code does not converge due to the strong coupling between phases; hence, Euler–Lagrange results are only presented for the finite-Stokes-number flow. For all simulations, the same uniformly spaced computational grid, composed of 40 cells in the wall-normal direction and 400 cells in the periodic direction, was used. The fluid phase equations have been discretized in space using the second-order accurate superbee scheme implemented into MFIX in both the two-fluid and QMOM simulations. The same discretization scheme was used for the particle phase equations in two-fluid simulations, while the moments transport equations are resolved using the procedure described in this work.

## 5. Results and discussion

### 5.1. Low-Stokes-number flow

The phase velocity profiles in the direction orthogonal to the channel walls predicted by the MFIX-QMOM simulations for the low-Stokes-number flow are reported in Figs. 3(a) and (b), for the partial and fully coupled cases, respectively. It is worth noting that the velocity profiles are not time-averaged, rather they are the results obtained at $t = 10$ s, when the simulations reached steady state. Only stream-wise profiles are reported for the MFIX-QMOM simulations, because they are identical along the length of the periodic channel. The two-fluid model predicts uniform property fields up to $t \approx 10$ s, then flow instabilities start to develop from the zone near the wall and quickly propagate to the rest of the system, which never reaches a steady state. It is worth to notice that the predictions of the two-fluid model as implemented into MFIX is extremely sensitive to the numerical tolerances for used in the iterative solution procedure. The default value of the tolerances led to predict an early onset of the instability, while reducing the value of the numerical tolerances to $1 \times 10^{-14}$, very close to the machine precision, caused the instability to be translated in time, as shown in the reported results. The predictions of the two-fluid model at $t = 10$ s are reported in Figs. 3(b) and 5.

For the low-Stokes-number flow, the two phases have almost identical velocities, leading to a relatively small local particle Reynolds number $Re_p$ (see Fig. 4). This can be understood by considering the local Stokes number $St_p$, defined by

$$St_p = \frac{\tau_p}{\tau_f} = \frac{\rho_p d_p^2 |\mathbf{U}_f|}{18 \mu_f D}, \tag{47}$$

where $\tau_p$ is the particle relaxation time, corresponding to the time required to adapt to a change in the local fluid velocity field, and $\tau_f$ is the characteristic time scale of the fluid ($D/|\mathbf{U}_f|$). The values of the local Stokes number in the MFIX-QMOM simulations are reported in Fig. 4, which shows that $St_p \leq 0.1$, indicating that the particles adapt relatively quickly to the fluid velocity field. Nevertheless, the local Stokes number near the center of the channel is large enough to allow for particle trajectory crossing, which can lead to unphysical delta shocks in two-fluid simulations. A similar trend to the one observed for the phase velocities is present in the particle-phase volume fraction profiles predicted by MFIX-QMOM (Fig. 5(a)), which again are unchanged along the height of the computational domain. In both the partial and fully coupled cases, the granular temperature profiles predicted by MFIX-QMOM (Fig. 5(b)) show a temperature peak very close to the wall, and significantly lower values at the center of the channel. This is justified by the fact that in the zone next to the wall, particles hit the wall and get reflected, giving origin to an increase in the particle velocity variance, since the net flux of particles is zero, but the particle velocity abscissas are not null. Overall, the local rms particle velocity (proportional to $\Theta^{1/2}$) is small compared to the mean particle velocity in all of the simulations. This fact implies that the local particle Mach number, defined by

$$Ma_p = \frac{|\mathbf{U}_p|}{\Theta^{1/2}}, \tag{48}$$

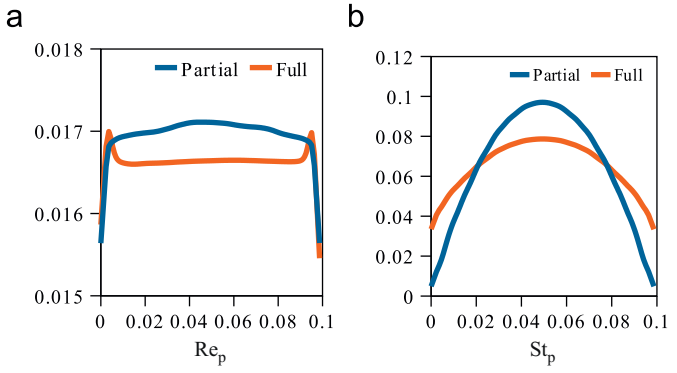


**Fig. 4.** (a) Local particle Reynolds number and (b) local Stokes number predicted by MFIX-QMOM for low-Stokes-number flow at $t = 10$ s.

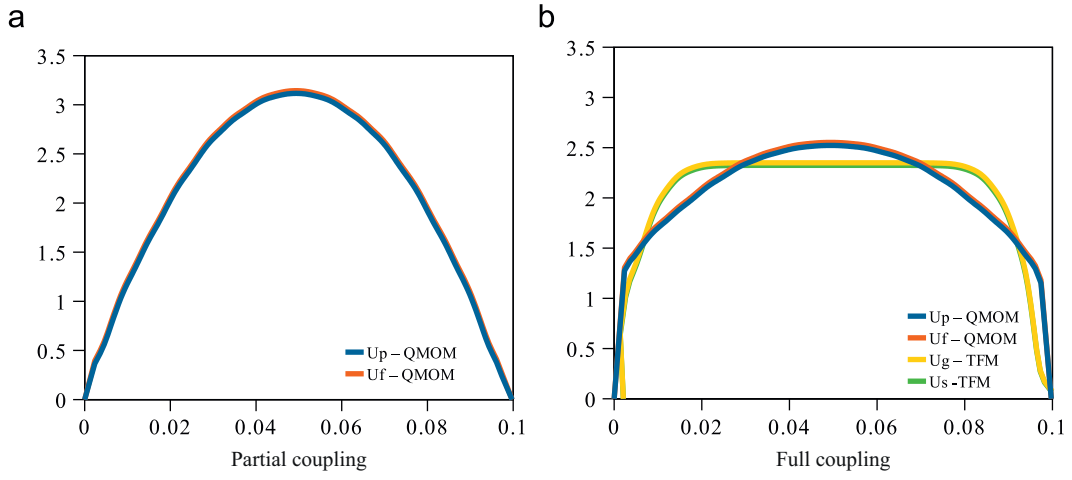


**Fig. 3.** Phase velocities (m/s) predicted by MFIX-QMOM and two-fluid model (TFM) for low-Stokes-number flow at $t = 10$ s.

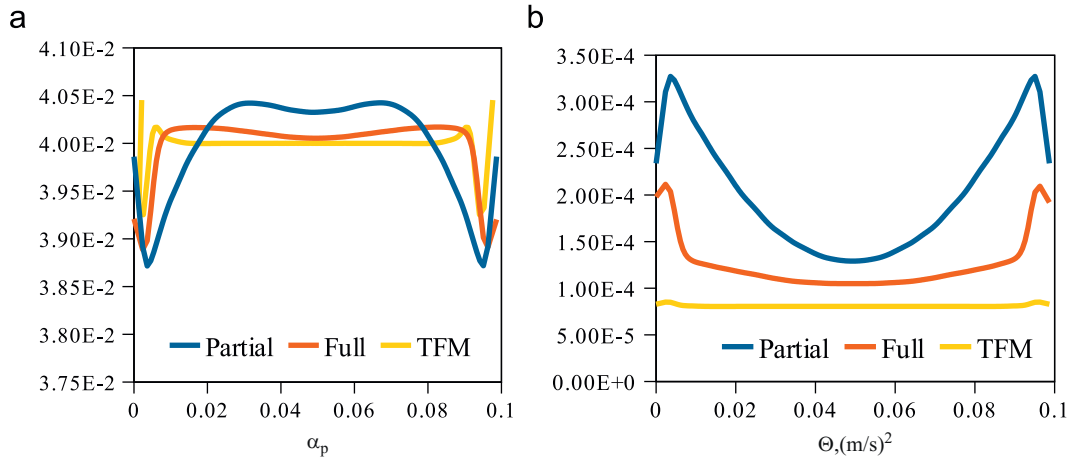


**Fig. 5.** (a) Particle-phase volume fraction and (b) granular temperature predicted by MFIX-QMOM and two-fluid model (TFM) for low-Stokes-number flow at $t = 10$ s.

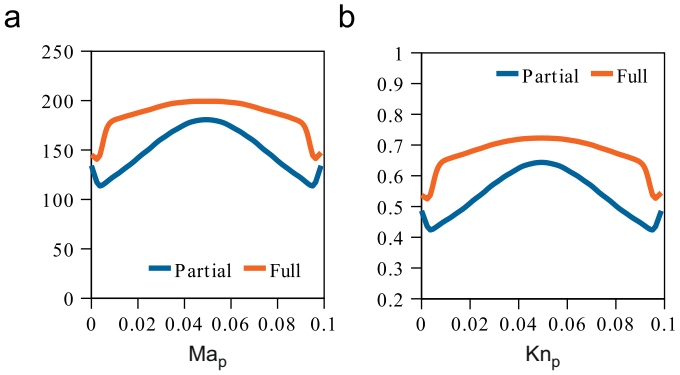


**Fig. 6.** Local particle Mach (a) and Knudsen (b) numbers predicted by MFIX-QMOM for low-Stokes-number flow at $t = 10$ s.

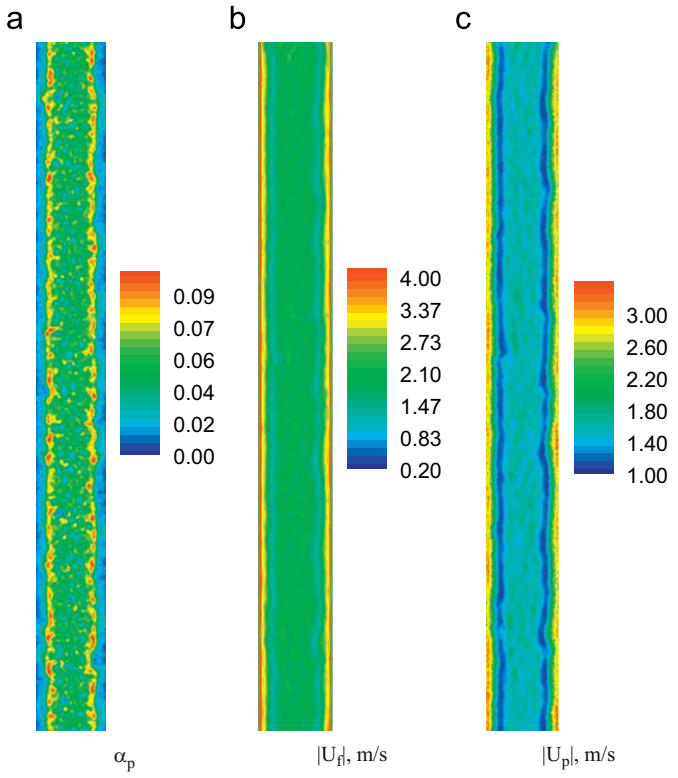


**Fig. 7.** Instantaneous contour plots of (a) the particle volume fraction, (b) the fluid-phase velocity magnitude and (c) the particle-phase velocity magnitude predicted by the Euler–Lagrange simulations at time $t = 0.19$ s for finite-Stokes-number flow.

is very large (see Fig. 6(a)), indicating that hydrodynamic models for the particle phase are likely to fail (Struchtrup, 2005). The granular temperature profile predicted by the two-fluid model does not show temperature peaks next to the walls, due to the presence of a Knudsen layer. This can be justified by observing that the Johnson and Jackson (1987) boundary conditions in the case of reflective walls corresponds to set the granular temperature flux to zero. In other words, the two-fluid model lacks of a mechanism to convert the impinging particle velocity into granular energy, even if the wall-normal velocity is null. This might also explain the differences in the shape of the velocity profiles observed in Fig. 3(b).

Better insight into the flow characteristics can be achieved by considering the local particle Knudsen number written for high Mach number flows[4] (Kogan, 1969) in terms of the local collision time $\tau_c$ (Eq. (20)) as

$$Kn_p = \sqrt{\frac{\pi}{2}}\frac{\tau_c|\mathbf{U}_p|}{D} = \frac{\pi d_p|\mathbf{U}_p|}{12\sqrt{2}Dg_0\alpha_p\Theta^{1/2}} \propto \frac{1}{\alpha_p}Ma_p, \tag{49}$$

where $\lambda_p$ is the particle mean free path. Note that the particle Knudsen number will be large if either the flow is very dilute, or if the particle Mach number is large. As shown in Fig. 6(a), in this flow $Ma_p$ is relatively large due to the low granular temperature. The profiles of the local particle Knudsen number from the MFIX-QMOM simulations are reported in Fig. 6(b). The values of the local particle Knudsen number are well outside the slip regime, where rarefaction effects can be described using partial slip boundary conditions (Bird, 1994; Rosner and Papadopoulos, 1996; Struchtrup, 2005). For values of $Kn_p > 0.1$, higher-order approximations of the kinetic equation are necessary, because the rarefaction effects extend inside the bulk of the system (Bird, 1994; Galvin et al., 2007). The particle Knudsen

[4] In the case of low Mach number flows ($Ma_p \leq 1$) the characteristic velocity of the particles is given by the square root of the granular temperature, leading to a different definition of the Knudsen number $Kn_p = \pi d_p/(12\sqrt{2}Dg_0\alpha_p)$. However, for high Mach number flows ($Ma_p > 1$) like those considered in this work, the characteristic velocity of the particles is the mean particle velocity.

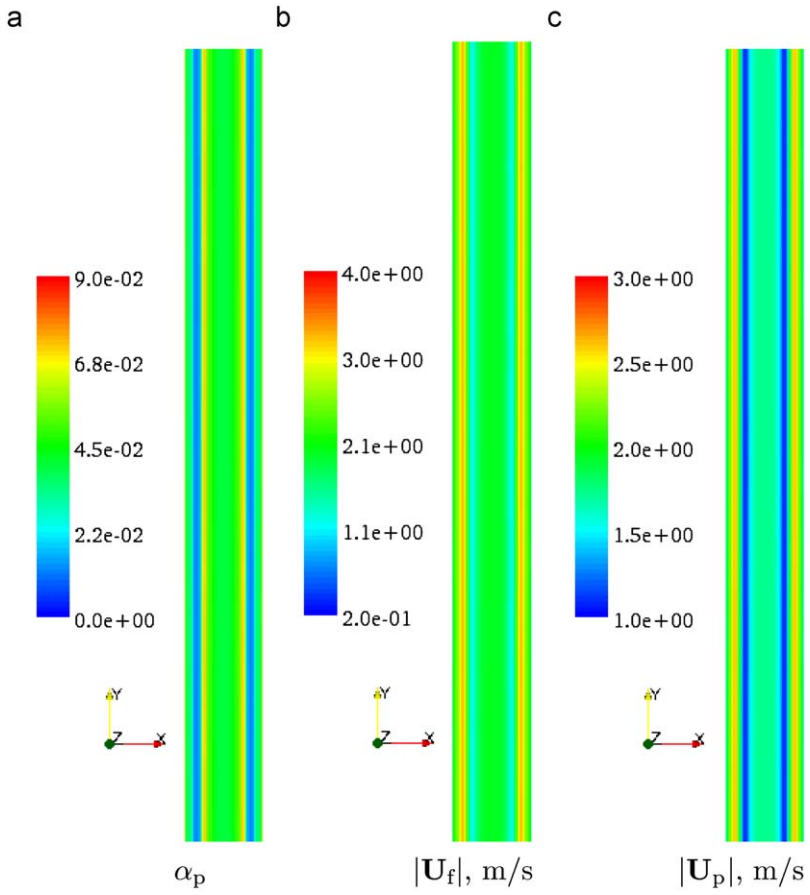


**Fig. 8.** Instantaneous contour plots of (a) the particle volume fraction, (b) the fluid-phase velocity magnitude and (c) the particle-phase velocity magnitude predicted by the MFIX-QMOM simulations at time $t = 0.66$ s for finite-Stokes-number flow.

number is inversely proportional to the rms particle velocity, and to the particle-phase volume fraction. In the situation considered in this work, the granular temperature is relatively low, leading to a small number of collisions, even though the particle-phase volume fraction is not particularly small.

In light of these observations, it is worth reconsidering the formation of transient structures with high particle concentration in gas–solid risers. In order to transport the solid particles, risers operate under highly turbulent conditions (i.e., $1 \ll Re_f$), where vortical structures typical of fully developed turbulent flow are known to induce particle segregation and cluster formation. For the low-Stokes-number flow, the fluid velocity was purposely restricted to laminar conditions, as is evident from the fluid velocity profile in the partially coupled case, which has the well-known parabolic shape. As a consequence, the phenomenon of particle segregation induced by the fluid turbulence is excluded. Nevertheless, the local Knudsen and Mach numbers for the particle phase are sufficiently large to expect non-equilibrium effects to be important. As a consequence, to properly predict the behavior of the particle phase when particle collisions are not dominant (e.g., very dilute flows or large particle Mach number), it is necessary to adopt methods that can resolve non-equilibrium phenomena, such as the Euler–Lagrange approach or the quadrature-based moment method.

### 5.2. Finite-Stokes-number flow

The results obtained with MFIX-QMOM for finite-Stokes-number flow are validated against Euler–Lagrange and two-fluid model predictions in this section. Due to the intrinsic noise of Euler–Lagrange simulations, the characteristic instability of the flow, which is

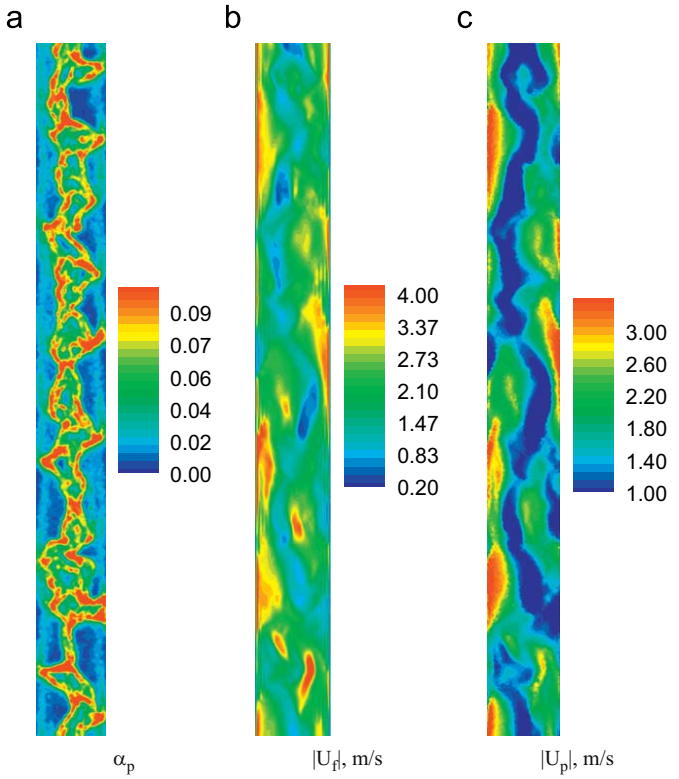


**Fig. 9.** Instantaneous contour plots of (a) the particle volume fraction, (b) the fluid-phase velocity magnitude and (c) the particle-phase velocity magnitude predicted by the Euler–Lagrange simulations at time $t = 0.44$ s for finite-Stokes-number flow.

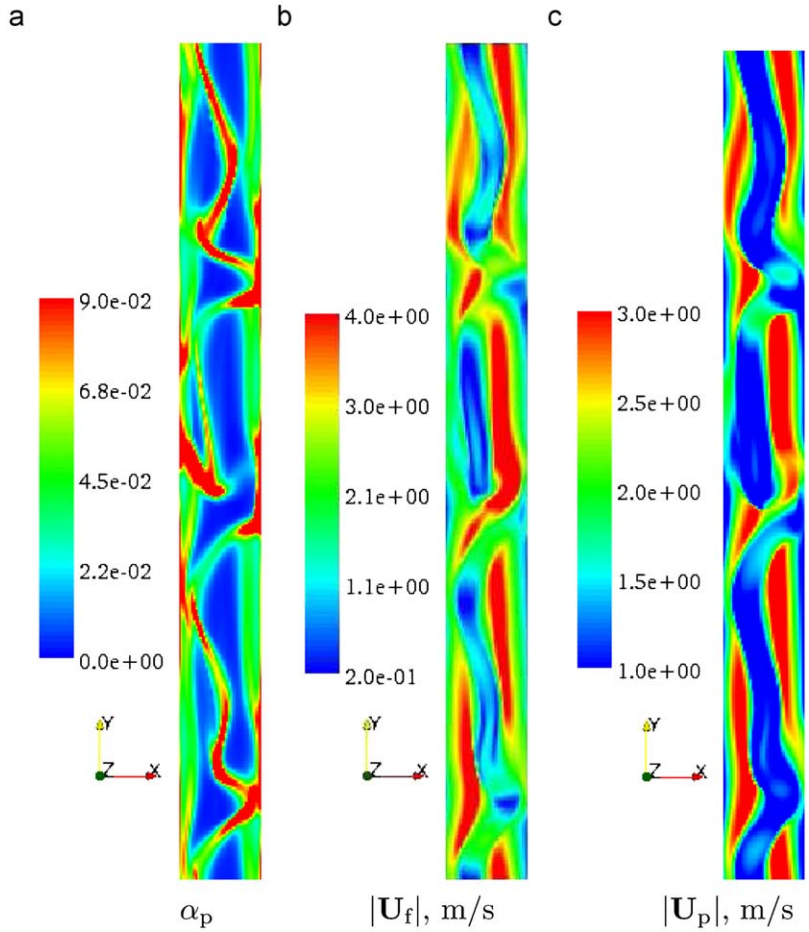


**Fig. 10.** Instantaneous contour plots of (a) the particle volume fraction, (b) the fluid-phase velocity magnitude and (c) the particle-phase velocity magnitude predicted by the MFIX-QMOM simulations at time $t = 1.20$ s for finite-Stokes-number flow.

discussed later, appears earlier than in MFIX-QMOM simulations. As a consequence, we shall compare property fields predicted by Euler–Lagrange and MFIX-QMOM at different times. On the other hand, the two-fluid model results are compared with MFIX-QMOM results at the same times.

*5.2.1. Euler–Lagrange and MFIX-QMOM comparison*

The results provided by Euler–Lagrange simulations at $t = 0.19$ s are reported in Fig. 7, and the corresponding MFIX-QMOM predictions at $t = 0.66$ s are shown in Fig. 8. The snapshots correspond to the phase immediately following the beginning of the simulation, when particles start to move away from the walls towards the center of the channel because they are reflected by the wall. This leads to the formation of two strips almost parallel to the walls, where the fluid velocity reaches its maximum value. Two bands at higher particle concentration start to form on the internal side with respect to the channel centerline of the two strips at higher void fraction. When the particle concentration in the two bands shown in Fig. 8(a) is high enough to create a consistent interface between the zone at lower particle concentration and the one at higher particle concentration, due to the large velocity gradient across the interface between the two phases, an instability starts to develop, which rapidly propagates to the rest of the system and, in the end, leads to the formation of structures at higher particle concentration, initiating the segregation phenomena experimentally observed in risers. This is shown for Euler–Lagrange and MFIX-QMOM simulations, respectively, in Figs. 9 ($t = 0.44$ s) and 10 ($t = 1.20$ s). Overall, the flow structures observed before (Figs. 7 and 8) and after (Figs. 9 and 10) the flow becomes highly transient are very similar in the MFIX-QMOM and Euler–Lagrange simulations.

*5.2.2. Two-fluid model and MFIX-QMOM comparison*

The two-fluid model predictions at $t = 1.15$ s are reported in Fig. 11, and can be compared with MFIX-QMOM results, taken at $t = 1.15$ s, reported in Fig. 12. Note that in both models, the same radial distribution function $g_0$ and modified drag law (Wen and Yu, 1966) are employed. In this case the particle volume fraction field presents a similar behavior in both MFIX-QMOM and two-fluid predictions, following the mechanism that leads to the development of the flow instability observed in the Lagrangian simulation. The propagation of the instability in MFIX-QMOM simulations is significantly influenced by the introduction of the radial distribution function $g_0$ and the modified drag coefficient, which make the instability propagate more quickly when a high enough volume fraction is reached locally. However, this does not alter the overall mechanism that leads to the instability and to the consequent segregation phenomena.

The local Knudsen, Stokes and Mach numbers predicted by QMOM simulations are reported in Fig. 13. In this figure, the local dimensionless numbers are plotted at $t = 1.15$ s, which corresponds to the instant where the Knudsen and Mach number show their minimum values (i.e., are closest to the hydrodynamic limit), before increasing due to the development of the instability. The Knudsen number locally reaches values well above the range of validity of

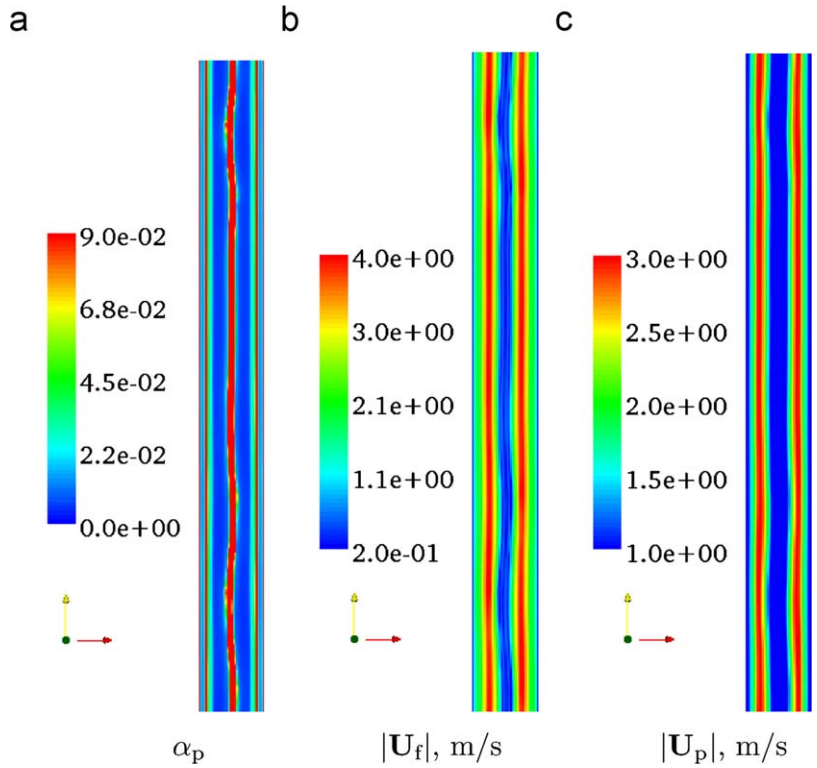


**Fig. 11.** Instantaneous contour plots of (a) the particle volume fraction, (b) fluid-phase velocity and (c) the particle-phase velocity at $t = 1.15$ s, predicted by the MFIX two-fluid model for finite-Stokes-number flow.

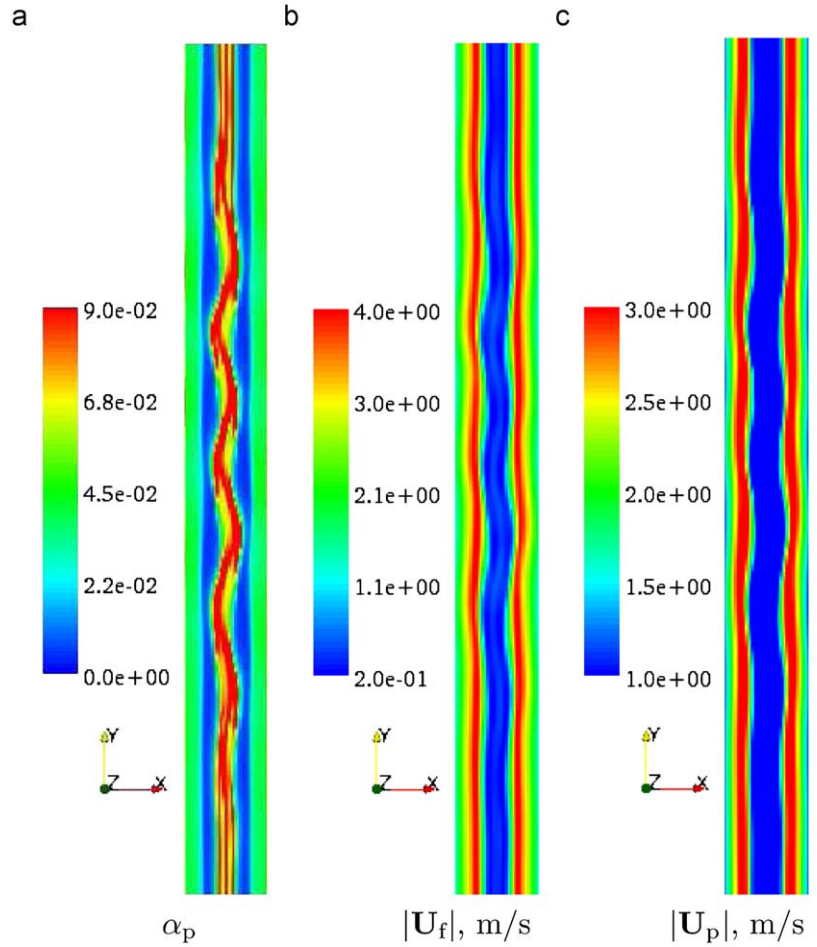


**Fig. 12.** Instantaneous contour plots of (a) the particle volume fraction, (b) the fluid-phase velocity magnitude and (c) the particle-phase velocity magnitude predicted by the MFIX-QMOM simulations at time $t = 1.15$ s for finite-Stokes-number flow.

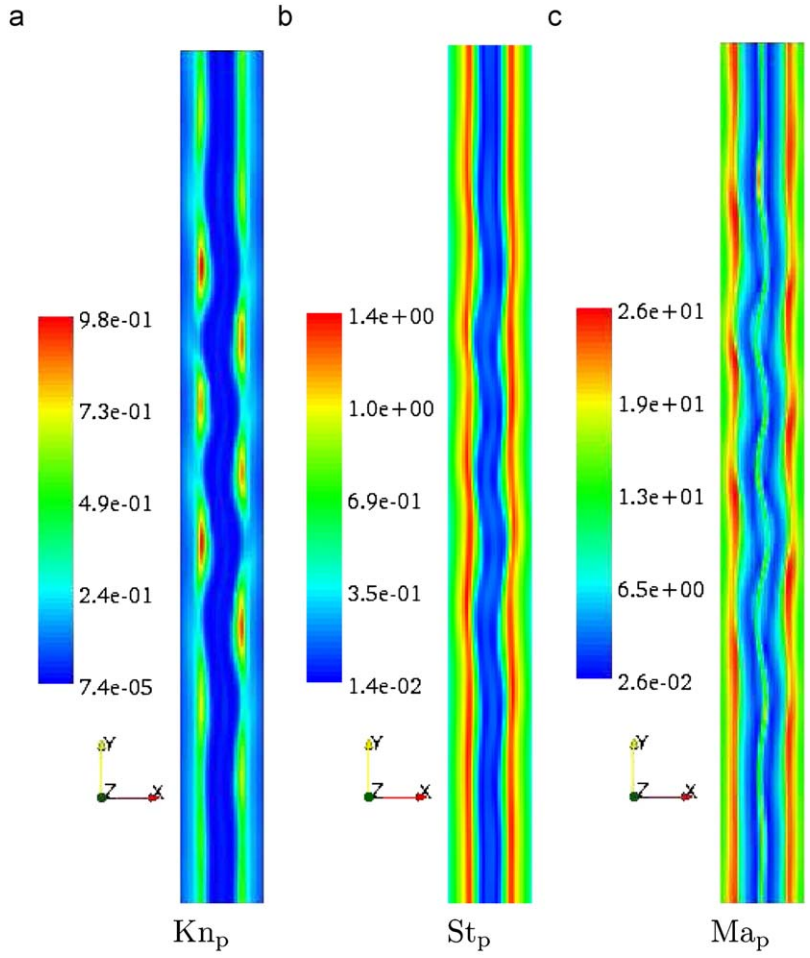


**Fig. 13.** Instantaneous contour plots of the local (a) Knudsen number, (b) Stokes number and (c) Mach number at $t=1.15$ s, predicted by MFIX-QMOM for finite-Stokes-number flow.

the two-fluid model ($Kn_p \ll 1$) and the particle Stokes number is about 10 times higher than in the low-Stokes-number flow, due to the larger particle diameter, with peak values near 1.4. This means that in certain regions of the finite-Stokes-number flow, particles do not adapt immediately to the fluid flow, and lead to the typical conditions where particle trajectory crossing becomes significant. Likewise, outside the central core region where the particle volume fraction is relatively high, the particle Mach number is very large. Under these conditions, one cannot expect a classical hydrodynamic model to yield accurate predictions (Struchtrup, 2005).

It is worth to observe this value of particle concentration corresponds to an average collision time of $1.78 \times 10^{-2}$ s, calculated considering a granular temperature of $10^{-4}$ m$^2$/s$^2$ and the average value of the volume fraction 0.04. This value if consistent with the observations about the Knudsen number we made with respect to the low Stokes number case. However, the collision time can be significantly lower locally, where the particle concentration increases due to segregation phenomena, as a consequence, it is necessary to account for collisions also in dilute cases like those examined in this work.

## 6. Conclusions

A quadrature-based moment method for the solution of the kinetic equation describing the evolution of a particle phase was coupled with a fluid solver to simulate the behavior of fully coupled fluid–particle flows. The applicability and the capabilities of the MFIX-QMOM code were discussed in comparison to CFD codes that use the classical two-fluid model. A vertical particle-laden channel flow with elastic collisions was used to demonstrate the robustness of the computational algorithm.

In general, we have shown that it is important to consider the local particle Knudsen number when simulating fluid–particle flows. The classical two-fluid model is applicable for cases where the particle Knudsen number is relatively small. We have seen that the particle Knudsen number will be large if either the particle-phase volume fraction is very small or the particle Mach number is large. Due to the dissipation of granular temperature by fluid–particle drag and inelastic collisions, it is likely that the particle Mach number will be large in many fluid–particle flows.

Finally, the objective of future work is to extend the QMOM approach to account for finite size particles, and deal with the denser cases, where it is necessary to enforce the constraint represented by the maximum value of the particle volume fraction. Note that, even for dilute riser flows, the particle phase can be locally dense, thus the code for simulating riser flows must be able to handle dense cases.

## Acknowledgments

This work was supported by a Grant (DE-FC26-07NT43098) from the National Energy Technology Laboratory (NETL) of the US Department of Energy. The authors would like to express their gratitude

to the two anonymous reviewers for their suggestions in improving the content and the clarity of this work.

## Appendix A. The moment-inversion algorithm

The moment-inversion algorithm is key to the quadrature-based moment method, because it allows the weights and abscissas in $V_8$ to be found from the moments $W^3$. The procedure is summed up here, and further details can be found in Fox (2008). The first step is to consider the mean particle velocity vector and the particle velocity covariance matrix:

$$\mathbf{U}_\mathrm{p} = \frac{1}{M^0}[M_1^1, M_2^1, M_3^1]^\mathrm{T}, \tag{50}$$

$$\boldsymbol{\sigma}_U = \begin{bmatrix} M_{11}^{2'} - U_{\mathrm{p}1}^2 & M_{12}^{2'} - U_{\mathrm{p}1}U_{\mathrm{p}2} & M_{13}^{2'} - U_{\mathrm{p}1}U_{\mathrm{p}3} \\ M_{12}^{2'} - U_{\mathrm{p}1}U_{\mathrm{p}2} & M_{22}^{2'} - U_{\mathrm{p}2}^{2'} & M_{23}^{2'} - U_{\mathrm{p}2}U_{\mathrm{p}3} \\ M_{13}^{2'} - U_{\mathrm{p}1}U_{\mathrm{p}3} & M_{23}^{2'} - U_{\mathrm{p}2}U_{\mathrm{p}3} & M_{33}^{2'} - U_{\mathrm{p}3}^2 \end{bmatrix}, \tag{51}$$

where $M_{ij}^{2'} = M_{ij}^2/M^0$. To perform the inversion of the set of moments in $W^3$, we introduce the vector

$$\mathbf{X} = A^{-1}(\mathbf{v} - \mathbf{U}_\mathrm{p}), \tag{52}$$

where $A$ is a linear transformation defined as the lower Cholesky decomposition of the covariance matrix $\boldsymbol{\sigma}_U$. The moments in $W^3$ are then normalized with respect to the vector $\mathbf{X}$, and the set of normalized moments $W_i^{3*}$ is defined for each component of $\mathbf{X}$:

$$W_i^{3*} = \{m_i^0 = 1, m_i^1 = 0, m_i^2 = 1, m_i^3\}. \tag{53}$$

Weights and abscissas in each direction are found by applying the two-node quadrature formulas to the three sets of pure normalized moments with respect to the directions:

$$\begin{aligned} n_{i1} &= 0.5 + \gamma_i, \quad X_{i1} = -\sqrt{\frac{1-2\gamma_i}{1+2\gamma_i}}, \\ n_{i2} &= 0.5 - \gamma_i, \quad X_{i2} = +\sqrt{\frac{1+2\gamma_i}{1-2\gamma_i}}, \end{aligned} \tag{54}$$

where

$$\gamma_i = \frac{0.5 m_i^3}{\sqrt{4 + (m_i^3)^2}}. \tag{55}$$

This operation provides the univariate sets of weights and abscissas:

$$\begin{aligned} V_1^* &= \{n_{11}, X_{11}; n_{12}, X_{12}\}, \\ V_2^* &= \{n_{21}, X_{21}; n_{22}, X_{22}\}, \\ V_3^* &= \{n_{31}, X_{31}; n_{32}, X_{32}\}. \end{aligned} \tag{56}$$

The three-dimensional quadrature approximation is defined then using the tensor product of the univariate abscissas, leading to the definition of $V_\beta^*$:

$$\begin{aligned} V_8^* = [&(n_1^*, X_{11}, X_{21}, X_{31}), (n_2^*, X_{12}, X_{21}, X_{31}), \\ &(n_3^*, X_{11}, X_{22}, X_{31}), (n_4^*, X_{12}, X_{22}, X_{31}), \\ &(n_5^*, X_{11}, X_{21}, X_{32}), (n_6^*, X_{12}, X_{21}, X_{32}), \\ &(n_7^*, X_{11}, X_{22}, X_{32}), (n_8^*, X_{12}, X_{22}, X_{32})]. \end{aligned} \tag{57}$$

The weights $n_i^*$ have to be determined by imposing the constraints given by the univariate nodes, by solving the linear system of equations:

$$\begin{aligned} n_1^* + n_3^* + n_5^* + n_7^* &= n_{11}, \\ n_2^* + n_4^* + n_6^* + n_8^* &= n_{12}, \\ n_1^* + n_2^* + n_5^* + n_6^* &= n_{21}, \\ n_3^* + n_4^* + n_7^* + n_8^* &= n_{22}, \\ n_1^* + n_2^* + n_3^* + n_4^* &= n_{31}, \\ n_5^* + n_6^* + n_7^* + n_8^* &= n_{32}, \end{aligned} \tag{58}$$

whose rank is four because $n_{i1} + n_{i2} = 1$ for $i = 1, 2, 3$. As a consequence, four additional equations are required, three of which are obtained by observing that the three second-order normalized cross moments $X_i X_j$ are zero, due to the linear transformation applied at the beginning of the procedure, and the fourth equation is obtained by writing the third-order moment $X_1 X_2 X_3$ in terms of the weights and abscissas, since its value is known. With the solution of the set of eight linear equations obtained above, the inversion algorithm is defined, and it is possible to compute $V_8$ from $W^3$.

It is worth to notice that all 20 moments tracked by Eq. (11) are required to define the moments inversion algorithm that allows the weights and abscissas to be found:

- The 10 pure moments in each spatial direction ($m_{000}$, $m_{100}$, $m_{010}$, $m_{001}$, $m_{200}$, $m_{020}$, $m_{002}$, $m_{300}$, $m_{030}$, $m_{003}$) are required to find the univariate weights $n_{ij}$ and abscissas $X_{ij}$.
- The three second order cross moments $m_{110}$, $m_{101}$, $m_{011}$ and the third order cross moment $m_{111}$ are used to obtain a linear system for the multivariate weights with a unique solution.
- The remaining six moments ($m_{210}$, $m_{201}$, $m_{210}$, $m_{120}$, $m_{102}$, $m_{021}$ and $m_{012}$) are required to have closed expressions of the other third order moments.

As a consequence, the set of moments required to define the quadrature approximation with two nodes for each spatial direction is exactly made of the 20 considered elements.

## Appendix B. Dimensionless equations for laminar fully developed channel flow

In MFIX-QMOM the model equations are solved in dimensional form using the time-dependent solver described in Section 3. However, in order to clarify the physics, it is useful to consider the dimensionless model equations for the special case of laminar, fully developed channel flow. The equations are made dimensionless by using the average fluid velocity $\overline{U}_\mathrm{f}$, the fluid density $\rho_\mathrm{f}$, and the channel width $D$. Taking $x_2$ as the vertical direction and $x_1$ as the horizontal direction, in laminar fully developed channel flow gradients exist only in the $x_1$ direction. Likewise, the only non-zero components of phase velocities are $U_{\mathrm{f},2}(x_1)$ and $U_{\mathrm{p},2}(x_1)$. Note that the fluid and particle continuity equations are exactly satisfied in this case.

The steady-state dimensionless fluid momentum equation in the $x_2$ direction reduces to

$$\frac{1}{Re_\mathrm{f}} \frac{d}{dx_1^*}\left(\alpha_\mathrm{f} \frac{dU_{\mathrm{f},2}^*}{dx_1^*}\right) - \alpha_\mathrm{f} g^* + \gamma = \sum_{\alpha=1}^{\beta} n_\alpha \beta_{\mathrm{fp},\alpha}^* (U_{\mathrm{f},2}^* - U_{\alpha,2}^*), \tag{59}$$

where $x_1^* = x_1/D$, $U_{\mathrm{f},2}^* = U_{\mathrm{f},2}/\overline{U}_\mathrm{f}$, $g^* = g/(D\overline{U}_\mathrm{f})$, and $\gamma$ is the dimensionless pressure gradient used to produce a fixed value for $\overline{U}_\mathrm{f}$. The dimensionless drag coefficient is

$$\beta_{\mathrm{fp},\alpha}^* = \frac{3\alpha_\mathrm{f} C_D(Re_{\mathrm{p}\alpha}, \alpha_\mathrm{f})|\mathbf{U}_\alpha^* - \mathbf{U}_\mathrm{f}^*|}{4 d_\mathrm{p}^*}, \tag{60}$$

where $\mathbf{U}^*_\alpha = \mathbf{U}_\alpha/\overline{U}_\mathrm{f}$ and $d^*_\mathrm{p} = d_\mathrm{p}/D$. Using symmetry, it is easily shown that

$$\gamma = \overline{\alpha}_\mathrm{f} g^* + \frac{2}{Re_\mathrm{f}}\left[\alpha_\mathrm{f}\frac{dU^*_{\mathrm{f},2}}{dx^*_1}\right]_{x^*_1=0} + \sum_{\alpha=1}^{\beta}\int_0^1 n_\alpha \beta^*_{\mathrm{fp},\alpha}(U^*_{\mathrm{f},2} - U^*_{\alpha,2})\,dx^*_1, \quad (61)$$

where $\overline{\alpha}_\mathrm{f}$ is the average fluid volume fraction. The first term on the right-hand side of Eq. (61) is due to the weight of the fluid phase and the second is the viscous drag at the channel walls. The third term (which is usually the largest) is due to the weight of the particle phase. In the Stokes flow regime, the third term simplifies to

$$\gamma_\mathrm{p} = \frac{1}{St}\int_0^1 \alpha_\mathrm{p}(U^*_{\mathrm{f},2} - U^*_{\mathrm{p},2})\,dx^*_1, \quad (62)$$

where the Stokes number is defined by $St = Re_\mathrm{f}(d^*_\mathrm{p})^2/18$. Note that in order to attain a steady state, $\gamma_\mathrm{p}$ must be non-negative. In the other two directions, the fluid momentum equation yields

$$\sum_{\alpha=1}^{\beta} n_\alpha \beta^*_{\mathrm{fp},\alpha} U^*_{\alpha,1} = 0 \quad \text{and} \quad \sum_{\alpha=1}^{\beta} n_\alpha \beta^*_{\mathrm{fp},\alpha} U^*_{\alpha,3} = 0. \quad (63)$$

Note that Eq. (63) does not imply that the individual velocity abscissas are null (only the weighted averages). Finally, recall that $\alpha_\mathrm{p} = \sum_\alpha n_\alpha$ and that the no-slip boundary conditions for the fluid require $U^*_{\mathrm{f},2}(0) = U^*_{\mathrm{f},2}(1) = 0$.

The particle-phase moment equations are made dimensionless using the same characteristic velocity and length scales as used for the fluid phase. In general, the moments of order $n$ have units of (velocity)$^n$. Thus, such moments are made dimensionless by dividing them by $\overline{U}^n_\mathrm{f}$. For laminar fully developed channel flow, the dimensionless moment equations reduce to

$$\frac{d\alpha_\mathrm{p} U^*_{\mathrm{p},1}}{dx^*_1} = 0, \quad (64)$$

$$\frac{dM^{2*}_{1i}}{dx^*_1} = \frac{D}{\overline{U}^2_\mathrm{f}} F^1_i, \quad (65)$$

$$\frac{dM^{3*}_{1ij}}{dx^*_1} = \frac{D}{\overline{U}^3_\mathrm{f}}(C^2_{ij} + F^2_{ij}), \quad (66)$$

$$\frac{dM^{4*}_{1ijk}}{dx^*_l} = \frac{D}{\overline{U}^4_\mathrm{f}}(C^3_{ijk} + F^3_{ijk}). \quad (67)$$

The first expression can be integrated to find $U^*_{\mathrm{p},1} = 0$ (due to the zero flux of particles through the walls). Likewise, due to symmetry, $U^*_{\mathrm{p},3} = 0$ as well as $M^{2*}_{13}$, $M^{2*}_{23}$, $M^{3*}_{113}$, $M^{3*}_{123}$, $M^{3*}_{223}$ and $M^{3*}_{333}$. (Recall that $M^{4*}_{ijk1}$ is closed by quadrature.) Thus, there are a total of 12 non-zero moments. Note that the constraints on the mean particle velocity do not imply that the velocity abscissas are also null.

Starting with Eq. (65), the three components ($i = 1, 2, 3$) yield, respectively,

$$\rho^*_\mathrm{p}\frac{d\alpha_\mathrm{p}\sigma^*_{11}}{dx^*_1} = -\sum_{\alpha=1}^{\beta} n_\alpha \beta^*_{\mathrm{fp},\alpha} U^*_{\alpha,1} = 0, \quad (68)$$

$$\rho^*_\mathrm{p}\frac{d\alpha_\mathrm{p}\sigma^*_{12}}{dx^*_1} = \sum_{\alpha=1}^{\beta} n_\alpha \beta^*_{\mathrm{fp},\alpha}(U^*_{\mathrm{f},2} - U^*_{\alpha,2}) - \alpha_\mathrm{p}\rho^*_\mathrm{p} g^*, \quad (69)$$

$$\sum_{\alpha=1}^{\beta} n_\alpha \beta^*_{\mathrm{fp},\alpha} U^*_{\alpha,3} = 0, \quad (70)$$

where $\rho^*_\mathrm{p} = \rho_\mathrm{p}/\rho_\mathrm{f}$ and $\sigma^*_{ij} = \sigma_{ij}/\overline{U}^2_\mathrm{f}$. The right-hand sides of Eqs. (68) and (70) follow from Eq. (63). Integration of Eq. (68) yields that $\alpha_\mathrm{p}\sigma^*_{11}$ is constant (independent of $x^*_1$). We can use Eq. (59) to rewrite Eq. (69) as

$$\rho^*_\mathrm{p}\frac{d\alpha_\mathrm{p}\sigma^*_{12}}{dx^*_1} = \gamma + \frac{1}{Re_\mathrm{f}}\frac{d}{dx^*_1}\left(\alpha_\mathrm{f}\frac{dU^*_{\mathrm{f},2}}{dx^*_1}\right) - (\alpha_\mathrm{f} + \alpha_\mathrm{p}\rho^*_\mathrm{p})g^*. \quad (71)$$

Using symmetry at the walls and the centerline, $\sigma^*_{12}(0) = \sigma^*_{12}(1/2) = \sigma^*_{12}(1) = 0$. Integrating Eq. (71) yields[5]

$$\alpha_\mathrm{p}(x^*_1)\sigma^*_{12}(x^*_1) = \frac{\gamma}{2\rho^*_\mathrm{p}}(2x^*_1 - 1) + \frac{\alpha_\mathrm{f}(x^*_1)}{\rho^*_\mathrm{p} Re_\mathrm{f}}\frac{dU^*_{\mathrm{f},2}}{dx^*_1}(x^*_1) - \int_{x^*_1}^{1/2}\left(\frac{\alpha_\mathrm{f}}{\rho^*_\mathrm{p}} + \alpha_\mathrm{p}\right) g^*\,dx^*_1. \quad (72)$$

Evaluating this equation at $x^*_1 = 0$ yields an independent expression for $\gamma$. Comparing with Eq. (61) it follows that

$$\sum_{\alpha=1}^{\beta}\int_0^1 n_\alpha \beta^*_{\mathrm{fp},\alpha}(U^*_{\mathrm{f},2} - U^*_{\alpha,2})\,dx^*_1 = \overline{\alpha}_\mathrm{p}\rho^*_\mathrm{p} g^*, \quad (73)$$

i.e., the momentum exchange term is equal to the weight of the particles as stated earlier.

Returning to Eq. (71) and considering a case where the fluid has *free-slip* boundary conditions at the walls (so that the fluid velocity gradient is null), we find that

$$\rho^*_\mathrm{p}\frac{d\alpha_\mathrm{p}\sigma^*_{12}}{dx^*_1} = (\overline{\alpha}_\mathrm{f} + \overline{\alpha}_\mathrm{p}\rho^*_\mathrm{p})g^* - (\alpha_\mathrm{f} + \alpha_\mathrm{p}\rho^*_\mathrm{p})g^*. \quad (74)$$

The right-hand side of this expression will be null if the particles are uniformly distribution across the channel, in which case $\sigma^*_{12} = 0$. The latter implies that all fluxes in the $x_1$ direction would be null, and hence the granular temperature will go zero due to drag. This observation points out the crucial role of the fluid velocity gradients in generating the non-uniform particle fields for this flow.

The next set of equations comes from the four non-trivial terms in Eq. (66):

$$\rho^*_\mathrm{p}\frac{dM^{3*}_{111}}{dx^*_1} = -2\sum_{\alpha=1}^{\beta} n_\alpha \beta^*_{\mathrm{fp},\alpha} U^*_{\alpha,1} U^*_{\alpha,1} + \frac{\rho^*_\mathrm{p}\alpha_\mathrm{p}}{\tau^*_\mathrm{c}}(\sigma^*_{\mathrm{eq}} - \sigma^*_{11}), \quad (75)$$

$$\rho^*_\mathrm{p}\frac{dM^{3*}_{112}}{dx^*_1} = \sum_{\alpha=1}^{\beta} n_\alpha \beta^*_{\mathrm{fp},\alpha}(U^*_{\mathrm{f},2}U^*_{\alpha,1} - 2U^*_{\alpha,1}U^*_{\alpha,2}) - \frac{\rho^*_\mathrm{p}\alpha_\mathrm{p}}{\tau^*_\mathrm{c}}\sigma^*_{12}, \quad (76)$$

$$\rho^*_\mathrm{p}\frac{dM^{3*}_{122}}{dx^*_1} = 2\sum_{\alpha=1}^{\beta} n_\alpha \beta^*_{\mathrm{fp},\alpha}(U^*_{\mathrm{f},2} - U^*_{\alpha,2})U^*_{\alpha,2} - \rho^*_\mathrm{p} g^* U^*_{\mathrm{p},2} + \frac{\rho^*_\mathrm{p}\alpha_\mathrm{p}}{\tau^*_\mathrm{c}}(\sigma^*_{\mathrm{eq}} - \sigma^*_{22}), \quad (77)$$

$$\rho^*_\mathrm{p}\frac{dM^{3*}_{133}}{dx^*_1} = -2\sum_{\alpha=1}^{\beta} n_\alpha \beta^*_{\mathrm{fp},\alpha} U^*_{\alpha,3} U^*_{\alpha,3} + \frac{\rho^*_\mathrm{p}\alpha_\mathrm{p}}{\tau^*_\mathrm{c}}(\sigma^*_{\mathrm{eq}} - \sigma^*_{33}). \quad (78)$$

The dimensionless collision time, which is closely related to the local particle Knudsen number defined in the main text, is defined by

$$\tau^*_\mathrm{c} = \frac{\pi^{1/2} d^*_\mathrm{p}}{12\alpha_\mathrm{p} g_0 (\Theta^*)^{1/2}}, \quad (79)$$

where the dimensionless granular temperature is $\Theta^* = \Theta/\overline{U}^2_\mathrm{f}$. Eqs. (75)–(78) all have the same form, thus we will discuss the physical meaning of the terms in Eq. (78) as an example. The term on the

[5] We have used the fact that the gradient of the fluid velocity is null on the centerline.

left-hand side represents the granular energy flux in the $x_1$ direction for $\sigma^*_{33}$ away from locations where it is produced (e.g., near the walls). The first term on the right-hand side is the dissipation of granular energy by the fluid drag, which can be very significant for small Stokes numbers (i.e., for large $\beta^*_{\mathrm{fp},\alpha}$). The second term on the right-hand side is the redistribution of granular energy due to collisions. Note that for elastic collisions the sum of the diagonal redistribution terms is null (i.e., granular energy is conserved during elastic collisions). Examples of the moments plotted versus $x^*_1$ for a vertical channel flow can be found in Fox (2008).

In conclusion, we note that the fluid drag has two competing effects on the granular temperature in this flow. On the one hand, fluid drag is needed to produce granular energy through a non-zero $\sigma^*_{12}$ acting on the non-zero mean particle velocity gradient. (In other words, both $\sigma^*_{12}\neq 0$ and $dU_{\mathrm{p},2}/dx_1\neq 0$ result from fluid drag.) On the other hand, fluid drag dissipates granular energy. Thus, the steady-state granular temperature will be maximum for an intermediate value of the Stokes number, and go to zero in the two extremes ($St=0$ and $St=\infty$[6] ).

## Appendix C. Two-fluid model equations

The equations used in the two-fluid model simulations are briefly summarized up in this appendix. The reader is invited to refer, for example, to Gidaspow (1994) for further details on their derivation. The fluid phase continuity equations are identical to those reported in Section 2.1. For the particle phase, a continuity equation

$$\frac{\partial \alpha_\mathrm{p}\rho_\mathrm{p}}{\partial t}+\nabla(\alpha_\mathrm{p}\rho_\mathrm{p}\mathbf{U}_\mathrm{p})=0, \tag{80}$$

and a momentum equation

$$\frac{\partial}{\partial t}(\alpha_\mathrm{p}\rho_\mathrm{p}\mathbf{U}_\mathrm{p})+\nabla(\alpha_\mathrm{p}\rho_\mathrm{p}\mathbf{U}_\mathrm{p}\mathbf{U}_\mathrm{p}) = \nabla\cdot\boldsymbol{\tau}_\mathrm{p}-\alpha_\mathrm{p}\nabla p-\nabla P_\mathrm{p}+\alpha_\mathrm{p}\rho_\mathrm{p}\mathbf{g}+K_\mathrm{drag}(\mathbf{U}_\mathrm{p}-\mathbf{U}_\mathrm{p}) \tag{81}$$

are solved, where the solids stress tensor has the form

$$\bar{\bar{\tau}}_\mathrm{p}=\mu_\mathrm{p}[\nabla\mathbf{U}_\mathrm{p}+\nabla^T\mathbf{U}_\mathrm{p}]+(\lambda_\mathrm{p}-\tfrac{2}{3}\mu_\mathrm{p})(\nabla\cdot\mathbf{U}_\mathrm{p})\mathbf{I}. \tag{82}$$

The transport equation

$$\frac{3}{2}\left[\frac{\partial}{\partial t}(\alpha_s\rho_s\Theta_s)+\nabla(\alpha_s\rho_s\mathbf{U}_s\Theta_s)\right] = (-P_s\mathbf{I}+\boldsymbol{\tau}_s):\nabla\mathbf{U}_s+\nabla(\kappa_s\nabla\Theta_s)-\gamma_s+J_\mathrm{vis} \tag{83}$$

is solved to compute the granular temperature $\Theta_\mathrm{p}$. The particle phase shear viscosity is given by the sum of a collisional and a kinetic contribution (Gidaspow, 1994)

$$\mu_\mathrm{p}=\mu_\mathrm{p,col}+\mu_\mathrm{p,kin}, \tag{84}$$

where

$$\mu_\mathrm{s,col}=\frac{4}{5}\alpha_\mathrm{p}^2\rho_\mathrm{p}d_\mathrm{p}g_0(1+e_\mathrm{p})\left(\frac{\Theta_\mathrm{p}}{\pi}\right)^{1/2} \tag{85}$$

and

$$\mu_\mathrm{p,kin}=\frac{10\rho_\mathrm{p}d_\mathrm{p}\sqrt{\Theta_\mathrm{p}\pi}}{96g_0(1+e_\mathrm{p})}\left[1+\frac{4}{5}(1+e_\mathrm{p})\alpha_\mathrm{p}g_0\right]^2. \tag{86}$$

[6] For elastic collisions, the case with $St=\infty$ has no dissipation mechanism. Thus, the total granular energy in the system will remain unchanged from the initial conditions. For finite $St$, the system will achieve a steady state where production and dissipation balance.

The particle phase bulk viscosity is given by equation

$$\lambda_\mathrm{p}=\frac{4}{3}\alpha_\mathrm{p}^2\rho_\mathrm{p}d_\mathrm{p}g_0(1+e_\mathrm{p})\left(\frac{\Theta_\mathrm{p}}{\pi}\right)^{1/2}. \tag{87}$$

The particle pressure is calculated according to equation

$$P_\mathrm{p}=\rho_\mathrm{p}\alpha_\mathrm{p}\Theta_\mathrm{p}+2\rho_\mathrm{p}\alpha_\mathrm{p}^2g_0\Theta_\mathrm{p}(1+e_\mathrm{p}). \tag{88}$$

The conductivity of the granular energy is calculated as

$$\kappa_\mathrm{p}=\frac{150\rho_\mathrm{p}d_\mathrm{p}\sqrt{\Theta_\mathrm{p}\pi}}{384g_0(1+e_\mathrm{p})}\left[1+\frac{6}{5}g_0\alpha_\mathrm{p}(1+e_\mathrm{p})\right]^2 + 2\alpha_\mathrm{p}^2\rho_\mathrm{p}d_\mathrm{p}g_0(1+e_\mathrm{p})\left(\frac{\Theta_\mathrm{p}}{\pi}\right)^{1/2}, \tag{89}$$

while the dissipation of granular energy due to collision is given by

$$\gamma_\mathrm{p}=3(1-e_\mathrm{p}^2)\rho_\mathrm{p}\alpha_\mathrm{p}^2g_0\Theta_s\left[\frac{4}{d_\mathrm{p}}\sqrt{\frac{\Theta_\mathrm{p}}{\pi}}-\nabla\cdot\mathbf{U}_\mathrm{p}\right]. \tag{90}$$

Finally, the dissipation of granular energy due to viscous damping $J_{vis}$ is modeled as

$$J_\mathrm{vis}=-3K_\mathrm{drag}\Theta_\mathrm{p}. \tag{91}$$

### C.1. Boundary conditions

The boundary conditions for the granular phase were set according to Johnson and Jackson (1987), who developed partial slip boundary conditions for the velocity

$$\tau_\mathrm{p,w}=-\frac{\pi}{6}\frac{\alpha_\mathrm{p}}{\alpha_\mathrm{p,max}}\varphi\rho_s g_0\sqrt{3\Theta_\mathrm{p}}\mathbf{U}_\mathrm{p,w} \tag{92}$$

and for the granular temperature

$$q_{\Theta,\mathrm{p}}=\frac{\pi}{6}\frac{\alpha_\mathrm{p}}{\alpha_\mathrm{p,max}}\varphi\rho_\mathrm{p}g_0\sqrt{3\Theta_\mathrm{p}}|\mathbf{U}_\mathrm{p,w}|^2-\frac{\pi}{4}\frac{\alpha_\mathrm{p}}{\alpha_\mathrm{p,max}}(1-e_\mathrm{p,w}^2)\rho_\mathrm{p}g_0\sqrt{3\Theta_\mathrm{p}^3}, \tag{93}$$

where $\tau_\mathrm{p,w}$ and $q_{\Theta,\mathrm{p}}$ are, respectively, the stress and the granular energy flux at the wall. Is is worth to notice that, the boundary condition for the velocity degenerates in a free slip condition if the specularity coefficient $\varphi$ is set to zero. In the same way, setting $\varphi=0$ and $e_\mathrm{p,w}=1$, reduces Eq. (93) to a Neumann boundary condition (zero flux).

## Appendix D. Comparison of computational times

A comparison of the computational times required by the two-fluid model implemented into MFIX and of MFIX-QMOM to perform the simulation considered in this work is reported in Table 2. Computational times were evaluated by running each simulation on a single core of an Intel Xeon Processor with a clock frequency 3.0 GHz. The computational time required in the high-St case, run assuming only one-way coupling with the fluid reduces to 4.1 h, showing that an important role in the computational time is due to the fluid solver and to the coupling procedure.

**Table 2**
Computational times (hours) of two-fluid model and MFIX-QMOM.

| Case | Two-fluid | QMOM | Ratio (QMOM/TF) |
|---|---|---|---|
| Low-St | 193.9 | 66.99 | 0.35 |
| High-St | 1.5 | 5.76 | 3.84 |

## References


Agrawal, K., Loezos, P.N., Syamlal, M., Sundaresan, S., 2001. The role of meso-scale structures in rapid gas–solid flows. Journal of Fluid Mechanics 445, 151.

Arastoopour, H., 2001. Numerical simulation and experimental analysis of gas/solid flow systems: 1999 Fluor–Daniel plenary lecture. Powder Technology 119, 59–67.

Avidan, A.A., 1995. Fluid catalytic cracking. In: Grace, J.R., Avidan, A.A., Knowlton, T.M. (Eds.), Circulating Fluidized Beds. Blackie Academic & Professional, London, pp. 467–487 (Chapter 13).

Benyahia, S., Arastoopour, H., Knowlton, T.M., Massah, H., 2000. Simulation of particles and gas flow behavior in the riser section of a circulating fluidized bed using the kinetic theory approach for the particulate phase. Powder Technology 112, 24–33.

Beylich, A., 2000. Solving the kinetic equation for all Knudsen numbers. Physics of Fluids 12, 444–465.

Bhatnagar, P.L., Gross, E.P., Krook, M., 1954. A model for collisional processes in gases. I. Small amplitude processes in charged and neutral one-component systems. Physical Review 94, 511–525.

Bird, G.A., 1994. Molecular Gas Dynamics and the Direct Simulation of Gas Flows. Oxford University Press, Oxford.

Brereton, C., 1995. Combustion performance. In: Grace, J.R., Avidan, A.A., Knowlton, T.M. (Eds.), Circulating Fluidized Beds. Blackie Academic & Professional, London, pp. 369–416 (Chapter 10).

Carnahan, N.F., Starling, K.E., 1969. Equation of state for nonattracting rigid spheres. Journal of Chemical Physics 51 (2), 635–636.

Carrillo, J., Majorana, A., Vecil, F., 2007. A semi-Lagrangian deterministic solver for the semiconductor Boltzmann–Poisson system. Communications in Computational Physics 2 (5), 1027–1054.

Cercignani, C., Illner, R., Pulvirenti, M., 1994. The Mathematical Theory of Dilute Gases. Springer, Berlin.

Chapman, S., Cowling, T.G., 1961. The Mathematical Theory of Non-uniform Gases. second ed. Cambridge University Press, Cambridge.

De Wilde, J., Van Engelandt, G., Heynderickx, G.J., Marin, G.B., 2005. Gas–solids mixing in the inlet zone of a dilute circulating fluidized bed. Powder Technology 151, 96–116.

Desjardin, O., Fox, R.O., Villedieu, P., 2008. A quadrature-based moment method for dilute fluid–particle flows. Journal of Computational Physics 227, 2524–2539.

Drew, D.A., 1971. Averaged equations for two-phase flows. Studies in Applied Mathematics L (3), 205–231.

Dry, R.J., Beeby, C.J., 1995. Applications of cfb technology to gas–solid reactions. In: Grace, J.R., Avidan, A.A., Knowlton, T.M. (Eds.), Circulating Fluidized Beds. Blackie Academic & Professional, London, pp. 442–465 (Chapter 12).

Enwald, H., Peirano, E., Almstedt, A.E., 1996. Eulerian two-phase flow theory applied to fluidization. International Journal of Multiphase Flow 22, 21–66.

Ferziger, J.H., Peric, M., 2002. Computational Methods for Fluid Dynamics. Springer, Berlin.

Fox, R.O., 2008. A quadrature-based third-order moment method for dilute gas–particle flows. Journal of Computational Physics 227, 6313–6350.

Galvin, J.E., Hrenya, C.M., Wildman, R.D., 2007. On the role of the Knudsen layer in rapid granular flows. Journal of Fluid Mechanics 585, 73–92.

Garg, R., Narayanan, C., Lakehal, D., Subramaniam, S., 2007. Accurate numerical estimation of interphase momentum transfer in Lagrangian–Eulerian simulations of dispersed two-phase flows. International Journal of Multiphase Flow 33, 1337–1364.

Garg, R., Narayanan, C., Subramaniam, S., 2009. A numerically convergent Lagrangian–Eulerian simulation method for dispersed two-phase flows. International Journal of Multiphase Flow 35, 376–388.

Gidaspow, D., 1986. Hydrodynamics of fluidization and heat transfer: supercomputer modeling. Applied Mechanics Reviews 39, 1–22.

Gidaspow, D., 1994. Multiphase Flow and Fluidization. Academic Press, New York.

Grace, J.R., Bi, H., 1997. Introduction to circulating fluidized beds. In: Grace, J.R., Avidan, A.A., Knowlton, T.M. (Eds.), Circulating Fluidized Beds,first ed. Blackie Academic & Professional, London, pp. 1–20 (Chapter 1).

Grad, H., 1949. On the kinetic theory of rarefied gases. Communications on Pure and Applied Mathematics 2 (4), 331–407.

Hrenya, C.M., Sinclair, J.L., 1997. Effects of particle-phase turbulence in gas–solid flows. A.I.Ch.E. Journal 43 (4), 853–869.

Johnson, P.C., Jackson, R., 1987. Frictional–collisional constitutive relations for granular materials, with applications to plane shearing. Journal of Fluid Mechanics 176, 67–93.

Karema, H., Lo, S., 1999. Efficiency of interphase coupling algorithms in fluidized bed conditions. Computer and Fluids 28, 323–360.

Kogan, M.N., 1969. Rarified Gas Dynamics. Plenum Press, New York.

Marchisio, D.L., Fox, R.O., 2003. Implementation of the quadraturenext term method of moments in CFD codes for aggregation-breakage problems. Chemical Engineering Science 58 (15), 3337–3351.

Oliveira, P.J., Issa, R.I., 1994. On the numerical treatment of interphase forces in two-phase flow. Numerical Methods in Multiphase Flows 185, 131–140.

Patankar, S., 1980. Numerical Heat Transfer and Fluid Flow. Taylor & Francis, London.

Peirano, E., Delloume, V., Johnsson, F., Leckner, B., Simonin, O., 2002. Numerical simulation of the fluid dynamics of a freely bubbling fluidized bed: influence of the air supply system. Powder Technology 122, 69–82.

Peirano, E., Leckner, B., 1998. Fundamentals of turbulent gas–solid flows applied to circulating fluidized bed combustion. Progress in Energy and Combustion Science 24, 259–296.

Perthame, B., 1990. Boltzmann type schemes for compressible Euler equations in one and two space dimensions. SIAM Journal of Numerical Analysis 29 (1), 1–19.

Rosner, D.E., Papadopoulos, D., 1996. Jump, slip and creep boundary conditions at nonequilibrium gas/solid interfaces. Industrial and Engineering Chemistry Research 35, 3210.

Sakiz, M., Simonin, O., 1998. Numerical experiments and modeling of non-equilibrium effect in dilute granular flows. In: Brun, R., Campargue, R., Gatignol, R., Lengrand, J. (Eds.), 21st International Symposium on Rarefied Gas Dynamics. Cépadduès editions, Toulouse, France.

Schiller, L., Naumann, A., 1935. A drag coefficient correlation. V. D. I. Zeitung 77, 318–320.

Schmidt, D.P., Rutland, C.J., 2000. A new droplet collision algorithm. Journal of Computational Physics 164, 62–80.

Simonin, O., 1991. Prediction of the dispersed phase turbulence in particle-laden jets. In: 4th International Symposium on Gas–Solid Flows, vol. 121. ASME-FED, pp. 197–206.

Sinclair, J.L., Jackson, R., 1989. Gas–particle flow in a vertical pipe with particle–particle interaction. A.I.Ch.E. Journal 35, 1473–1486.

Spalding, D., 1980. Numerical computation of multi-phase fluid flow and heat transfer. In: Taylor, C. (Ed.), Recent Advances in Numerical Methods in Fluids. Pineridge Press,

Struchtrup, H., 2005. Macroscopic Transport Equations for Rarefied Gas Flows. Springer, Berlin.

Syamlal, M., 1998. MFIX Documentation Numerical Technique. U.S. Department of Energy, Office of Fossil Energy, Federal Energy Technology Center, Morgantown, WV.

Syamlal, M., Gidaspow, D., 1985. Hydrodynamics of fluidization: prediction of wall to bed heat transfer coefficient. A.I.Ch.E. Journal 31, 127–135.

Syamlal, M., Rogers, W., O'Brien, T.J., 1993. MFIX Documentation Theory Guide. U.S. Department of Energy, Office of Fossil Energy, Morgantown Energy Technology Center, Morgantown, WV.

Wen, C.Y., Yu, Y.H., 1966. Mechanics of fluidization. Chemical Engineering Progress Symposium Series 62, 100–111.